

1-1-2007

An experimental study of soil thermal conductivity using a guarded hot plate apparatus

Ivan Nikolaev
Ryerson University

Follow this and additional works at: <http://digitalcommons.ryerson.ca/dissertations>

 Part of the [Mechanical Engineering Commons](#)

Recommended Citation

Nikolaev, Ivan, "An experimental study of soil thermal conductivity using a guarded hot plate apparatus" (2007). *Theses and dissertations*. Paper 144.

80
525
155
2007

**AN EXPERIMENTAL STUDY OF
SOIL THERMAL CONDUCTIVITY
USING A GUARDED HOT PLATE APPARATUS**

by

Ivan Nikolaev

B.Eng. University of Toronto,
Canada 2005

A thesis presented to

Ryerson University

in partial fulfillment of the
requirements for the degree of
Master of Applied Science

in the Program of
Mechanical Engineering

Toronto, Ontario, Canada, 2007
© Ivan Nikolaev 2007

**PROPERTY OF
RYERSON UNIVERSITY LIBRARY**

AUTHOR'S DECLARATION

I hereby declare that I am the sole author of this thesis.

I authorize Ryerson University to lend this thesis to other institutions or individuals for the purpose of scholarly research.

I further authorize Ryerson University to reproduce this thesis by photocopying or by other means, in total or in part, at the request of other institutions or individuals for the purpose of scholarly research.

ABSTRACT

Ivan Nikolaev

An Experimental Study of Soil Thermal Conductivity
Using a Guarded Hot Plate Apparatus

Master of Applied Science
Mechanical Engineering

Ryerson University, Toronto, 2007

A guarded hot plate apparatus was used to generate comprehensive sets of thermal conductivity for two types of soils, namely Ottawa sand and Richmond Hill clay-loam, for temperature variation from 2 to 92°C and moisture content variation from complete dryness to full saturation with measurement errors of less than 3%. Numerical simulation of heat transfer within the apparatus with a sample inside was performed to validate the experimental design and setup. To prepare the samples, a consistent specimen preparation technique was developed for the cases of dry, barely-to-moderately moist, and highly-to-fully saturated moist soils. On the basis of gathered datasets, empirical correlations for soil thermal conductivity were developed as a function of moisture content for each experimental temperature and also as a function of both temperature and moisture content. The proposed correlations produced excellent fit to majority of the experimental data, and could be easily integrated into numerical analysis of underground heat transfer. As an application example, one of the correlations was employed to evaluate soil thermal conductivity in a numerical study of underground heat loss from a basement wall and floor, in order to illustrate the importance of considering the dependence of soil thermal conductivity on soil texture, temperature and degree of saturation.

ACKNOWLEDGEMENTS

The author would like to express his deepest appreciation to Dr. W. Leong and Dr. M. Rosen for their guidance and encouragement throughout the project.

The author wishes to thank the engineering support staff at Ryerson University. Particularly Joseph Amankrah and Alan Machin for their advice and assistance through the apparatus design modification phase of the project.

Finally, I wish to thank my family and friends for their patience and support over the past two years.

TABLE OF CONTENTS

	Page
AUTHOR'S DECLARATION	ii
ABSTRACT	iii
ACKNOWLEDGEMENTS	iv
TABLE OF CONTENTS	v
LIST OF FIGURES	viii
LIST OF TABLES.....	xi
NOMENCLATURE.....	xii
CHAPTER 1 - GENERAL REVIEW	
1.1 Introduction	1
1.2 Literature Review	5
1.2.1 Experimental Studies of Soil Thermal Conductivity	5
1.2.2 Modeling of Thermal Conductivity of Soils	8
1.3 Objectives and Scope of Research and Applications of Results.....	10
1.4 Outline of the Thesis	11
CHAPTER 2 - AN OVERVIEW OF RYERSON GUARDED HOT PLATE APPARATUS	
2.1 Introduction	13
2.2 Overview of GHP Operation Principles	13
2.2.1 Measurement of Thermal Conductivity	15
2.3 Overview of Modified GHP Apparatus	17
2.3.1 Plate Assembly	22
2.3.2 Automated Operation of GHP Apparatus	27
2.4 Calibration of GHP Apparatus	31
2.5 Experimental Error Analysis	31
CHAPTER 3 - NUMERICAL ANALYSIS OF THE GHP ASSEMBLY WITH A SOIL SPECIMEN	
3.1 Introduction to Numerical Model	33
3.2 Discretization of Computational Domain	36
3.3 Mathematical Formulation	38
3.3.1 Boundary Conditions	38
3.4 Grid Sensitivity Study	40
3.5 Analysis of Numerical Results	42

CHAPTER 4 - SOIL SAMPLE PREPARATION, PROPERTY MEASUREMENTS, AND EXPERIMENTAL PROCEDURES

4.1	Introduction	47
4.2	Preparation of Soil Samples	48
4.2.1	Preparation of Dry Soil Samples	48
4.2.2	Preparation of Barely-to-Moderately Moist Soil Samples.....	49
4.2.3	Preparation of Highly-to-Fully Saturated Moist Soil Samples.....	51
4.3	Properties and Composition of Experimental Soils	53
4.4	Experimental Planning and Procedure	55

CHAPTER 5 - PRESENTATION AND DISCUSSION OF EXPERIMENTAL RESULTS

5.1	Introduction.....	57
5.2	Experimental Results.....	58
5.3	Verification of Results.....	63
5.4	Reproducibility of the Experiment.....	64

CHAPTER 6 - DEVELOPMENT OF EMPIRICAL CORRELATIONS FOR THERMAL CONDUCTIVITY OF EXPERIMENTAL SOILS

6.1	Introduction.....	66
6.2	Development of an Empirical Correlation.....	66
6.3	Fitting Error of The Empirical Correlation.....	73
6.4	An Alternative Correlation Model.....	76

CHAPTER 7 - NUMERICAL SIMULATION OF HEAT TRANSFER FROM A BASEMENT SURROUNDED BY COARSE AND FINE SOILS OF DIFFERENT MOISTURE CONTENTS

7.1	Introduction.....	80
7.2	Discretization of Domain and Grid Sensitivity Study.....	81
7.3	Mathematical Formulation and Boundary Conditions.....	83
7.4	Heat Transfer: Effect of Thermal Conductivity Variation with Soil Texture, Moisture Content and Temperature.....	85

CHAPTER 8 - CONCLUSIONS AND RECOMMENDATIONS

8.1	Summary and Conclusions.....	91
8.2	Recommendations.....	94

APPENDIX A: Thermal conductivity of experimental soils with temperature and volumetric moisture content.....	95
References.....	98

LIST OF FIGURES

Figure	Description	Page
1.1	General outline of GHP apparatus.....	4
2.1	General schematic of a GHP apparatus.....	14
2.2	Assembly of hot plate, heater plate, and heat flux meter.....	16
2.3	The Ryerson GHP apparatus.....	19
2.4	Schematic of GHP plate assembly (hot plate is shown without the heater plate and heat flux meter) [11].....	23
2.5	Positions of thermocouples, thermopile, and RTD on the hot plate (top view) [11].....	24
2.6	Heater plate with a serpentine groove for nichrome wire. All dimensions are in mm [11].....	25
2.7	A complete assembly of the hot plate, the heater plate, and the heat flux meter in between [11].....	25
2.8	Block diagram of <i>GHP Control v.2.0</i> data acquisition software.....	30
3.1	Model of a GHP assembly including a container with soil specimen.....	35
3.2	Magnified view of a portion of the model showing details about the silicone rubber pads, the steel container, the heat flux meter and copper plates.....	36
3.3	Discretized domain with 2882 nodes and 7628 elements.....	37
3.4	Geometry and boundaries of the computational domain.....	40
3.5	Temperature field solution within the air gap region (right) with regard to coarse grid density (left).....	41
3.6	Temperature field solution within the air gap region (right) with regard to medium grid density (left).....	42
3.7	Temperature field solution within the air gap region (right) with regard to high grid density (left).....	42

3.8	Left: Temperature distribution within the computational domain for $\Delta T=10^{\circ}\text{C}$ between the hot and cold plates (highest isotherm at $T_h=T_{\text{htr}}=200^{\circ}\text{C}$, lowest isotherm at $T_c=190^{\circ}\text{C}$). Right: Temperature gradients.....	43
3.9	Temperature distribution within the computational domain for $\Delta T=5^{\circ}\text{C}$ between the hot and cold plates (highest isotherm at $T_h=T_{\text{htr}}=200^{\circ}\text{C}$, lowest isotherm at $T_c=195^{\circ}\text{C}$). Right: Temperature gradients.....	43
3.10	Temperature distribution within the computational domain for $\Delta T=2^{\circ}\text{C}$ between the hot and cold plates (highest isotherm at $T_h=T_{\text{htr}}=200^{\circ}\text{C}$, and lowest isotherm at $T_c=198^{\circ}\text{C}$). Right: Temperature gradients.....	44
3.11	Temperature variation of approximately 0.025°C within the hot and heater plates (on the left), and cold plate (on the right) at $\Delta T=10^{\circ}\text{C}$	45
3.12	Temperature variation of approximately 0.015°C within the hot and heater plates (on the left), and cold plate (on the right) at $\Delta T=5^{\circ}\text{C}$	45
3.13	Temperature variation of approximately 0.01°C within the hot and heater plates (on the left), and cold plate (on the right) at $\Delta T=2^{\circ}\text{C}$	45
4.1	Soil texture chart [39].....	54
5.1	Variation in thermal conductivity of Ottawa sand with temperature and volumetric moisture content.....	60
5.2	Variation in thermal conductivity of Richmond Hill soil with temperature and volumetric moisture content.....	61
5.3	Experimental and published thermal conductivity values of Ottawa sand.....	63
5.4	Reproducibility test, based on the Ottawa sand specimen with $0.33\text{ m}^3\text{m}^{-3}$ moisture content.....	64
6.1	Thermal conductivity vs. VMC for Ottawa sand with superimposed empirical correlation for various temperatures. Each experimental temperature considered from 2 to 92°C is shown from (a) to (j).....	69

6.2	Thermal conductivity vs. VMC for Richmond Hill clay-loam with superimposed empirical correlation for various temperatures. Each experimental temperature considered from 2 to 92°C is shown from (a) to (j).....	71
6.3	Tarnawski empirical correlation for thermal conductivity of Ottawa sand.....	79
6.4	Tarnawski empirical correlation for thermal conductivity of Richmond Hill clay-loam.....	79
7.1	Model of a basement surrounded by soil.....	81
7.2	Coarse grid density (left), and respective temperature field (right). 15 isothermal lines with $T_{\min}=0.28^{\circ}\text{C}$, $T_{\max}=20^{\circ}\text{C}$	82
7.3	Medium grid density (left), and respective temperature field (right). 15 isothermal lines with $T_{\min}=0.29^{\circ}\text{C}$, $T_{\max}=20^{\circ}\text{C}$	82
7.4	High grid density (left), and respective temperature field (right). 15 isothermal lines with $T_{\min}=0.29^{\circ}\text{C}$, $T_{\max}=20^{\circ}\text{C}$	82
7.5	Temperature distributions regarding Ottawa sand at different moisture contents. For simulations (a), (b), (c) the thermal conductivity is set as a function of temperature for a moisture content ($\lambda=f(T, \theta)$), but in (d), (e), (f) as a function of T_{ave} for a moisture content ($\lambda=f(T_{\text{ave}}, \theta)$).....	89
7.6	Temperature distributions regarding Richmond Hill clay-loam at different moisture contents. For simulations (a), (b), (c) the thermal conductivity is set as a function of temperature for a moisture content ($\lambda=f(T, \theta)$), but for (d), (e), (f) as a function of T_{ave} for a moisture content ($\lambda=f(T_{\text{ave}}, \theta)$).....	90

LIST OF TABLES

Table	Description	Page
2.1	GHP apparatus inventory list.....	20
2.2	Overall bias errors of measured quantities and $U_{0.95}$ of λ [31].....	32
3.1	Material properties used to model the components of the GHP assembly.....	36
4.1	Permanent wilting point, field capacity and full saturation points of Ottawa sand and Richmond Hill clay-loam.....	55
6.1	Temperature dependent correlation coefficients for Ottawa sand..	68
6.2	Temperature dependent correlation coefficients for Richmond Hill clay-loam.....	68
6.3	Statistical evaluation of the goodness of fit for the developed model (Equation (6.2)) for Ottawa sand (Table 6.1) and Richmond Hill clay-loam (Table 6.2).....	76
6.4	Tarnawski correlation coefficients for Ottawa sand and Richmond Hill clay-loam.....	77
7.1	Heat flows through below-grade wall and the floor with respect to coarse and fine soil textures at several moisture contents.	87
7.2	RPD in heat flow regarding variation of moisture content of Ottawa sand and Richmond Hill clay-loam.....	88
7.3	RPD between the heat flows regarding the thermal conductivity as a function of temperature and moisture content, and as a function of moisture content only (at $T_{ave}=10^{\circ}\text{C}$).....	89
A.1	Measured thermal conductivity (W/m·K) of Ottawa sand	96
A.2	Measured thermal conductivity (W/m·K) of Richmond Hill clay-loam.....	97

NOMENCLATURE

A	Cross-sectional area [m^2]
D	Diameter [m]
e	Heat flux meter <i>emf</i> output [mV]
FC	Field capacity
FS	Full saturation
GHP	Guarded hot plate
HFM	Heat flux meter
h	Heat transfer coefficient [W/m^2K]
I	Current [A]
L	Uniform thickness of the specimen [m]
M	Mass [kg]
m	Mass fraction
N	Number of
P	Electrical Power [W]
PRT	Platinum resistance thermometer
PWP	Permanent wilting point
q''	Heat flux [W/m^2]
q	Heat transfer rate [W or W/m]
RPD	Relative percentage difference [%]
RTD	Resistance temperature detector
T	Temperature [K or $^{\circ}C$]
t	Time [s]
U	Overall uncertainty
V	Volume [m^3]
VMC	Volumetric moisture content [m^3/m^3]
x,y,z	Cartesian co-ordinates [m]

Greek

α	Calibration proportionality constant for HFM [W/mV]
σ	Standard deviation
δT	Temperature difference between heater and hot plates [K or $^{\circ}C$]
ΔT	Temperature difference between heater and cold plates [K or $^{\circ}C$]
Δt	Time difference [s]
λ	Thermal conductivity [W/mK]
ρ	Density [kg/m^3]
θ	Volumetric moisture content [m^3/m^3]
ϕ	Porosity [m^3/m^3]

Subscripts

0.95	Associated with 95% confidence level
∞	Ambient
ave	Average value
c	Cold plate
cl	Clay
coarse	Coarse soil texture
cond	Conduction heat transfer
conv	Convective heat transfer
dry	Dry specimen
ds	Dry soil
db	Dry bulk
e	Electrical heater
est	Estimated value
exp	Experimental value
grid	Numerical discretization grid
fine	Fine soil texture
h	Hot plate
htr	Heater plate
inside	Inside property
m	Mean value
min	Minimum value
max	Maximum value
s	Specimen
sa	Sand
si	Silt
surface	Surface property
w	Water

CHAPTER
1
GENERAL REVIEW

1.1 Introduction

Many engineering, environmental, and agronomical applications require a precise estimate of soil thermal properties. The property often of the highest interest is effective thermal conductivity since it reflects the ability of soil to conduct heat, and as such is essential to solving problems related to ground waste disposal, geothermal energy extraction, enhanced oil recovery, ground thermal storage, thermal soil remediation, behavior of forest fires, the climate tuning of buildings to specific environments, etc [1-3].

Not surprisingly, numerous attempts have been made to develop advanced analytical techniques to predict quickly the thermal conductivity of soils, and although these approaches have significantly evolved over the past several decades, they are still not capable of precise estimation. There are two main reasons for this. Firstly, the inadequacy can be explained partially by the complexity of the model formulation itself, since the thermal conductivity of soil depends on numerous complex parameters (such as mineral composition, moisture, texture, porosity and particle size distribution, etc) which are difficult to

incorporate into a single model [4-6]. Secondly, in order to properly calibrate and verify an analytical model, reliable experimental data is required; meanwhile there is a lack of comprehensive and accurate experimental research, especially in cases of low moisture contents and temperatures beyond 60°C [4, 7]. It is important to note that only a few limited high temperature studies (up to and above 60°C) have been conducted. However they usually lack some important information about particle size distribution and textural composition of soil samples involved. Thus, in order to aid the development of more accurate analytical models of soil thermal conductivity, a more complete experimental dataset (including textural composition, particle size distribution as well as precise error analysis) must be gathered first.

There are two general experimental approaches to measure the thermal conductivity, namely transient and steady-state. Some examples of transient techniques are laser flash, hot wire, single and dual heated probes. The most commonly used amongst them are single and dual heated probes. The single probe method employs a heat source inserted into the specimen and heat is supplied to it continuously at a constant rate. The thermal properties are determined by analyzing the temperature response around the heat source. In particular, the technique is based on measuring the rate at which the heat is conducted away from the probe [8]. One of the limitations of the single probe technique is that it is only able to measure thermal conductivity. The dual-probe technique involves two parallel needle probes, one being a heater and the other a temperature sensor. When the heat pulse is applied, the temperature sensor

records the response as a function of time. Relative to the single probe approach, the benefit of dual probe technique is that it is able to measure both thermal diffusivity and volumetric heat capacity. From this, all the main soil thermal properties can be determined, including thermal conductivity [4, 7]. In general, most of the transient techniques are quick and portable, and require small soil specimens, and as such are commonly used in the field and industry. However, due to several drawbacks their results are often inadequate and deviate significantly from the actual thermal conductivity values. One of the reasons is the dependence on the probe-to-soil contact, when for example the air gap around the probe leads to a severe error. Moreover, high temperature measurements are especially prone to error because of the greater thermally induced moisture movement within the sample, caused by the temperature gradients from raising the temperature as well as from the probe line heat source. At temperatures above 60°C even a relatively small localized dryness around the probe can have a significant affect on the measurement of thermal conductivity, since the heat transport is governed by the latent heat at these temperatures. As a result, lower thermal conductivity measurements are common with probe techniques, since the probe is not a water source by itself, and the thermal conductivity is measured on the basis of the soil right around the probe, rather than within entire experimental container [2, 9].

Unlike the transient approaches, the steady-state approaches are bulky and much more time consuming, and demand care in lengthy experiments. They are based on a careful monitoring of heat inputs, precise temperature measurements,

and a definite heat flow pattern. Although the steady-state setup is more complex and the experimental methodology is more challenging, the results can be extremely accurate and, as such, they are the benchmark for transient techniques [9].

The present research is based on one particular steady-state technique called the Guarded Hot Plate (GHP) method, involving a monitored one-dimensional heat flux through a specimen which is fixed between parallel plates (refer to Figure 1.1). The upper plate is comprised of two elements: a heater plate and a hot plate which functions as a thermal guard for the heater plate. During experiments, the hot and heater plates are kept at the same temperature; however they are heated independently and are separated by a small gap to create a thermal barrier. The hot plate is maintained at slightly higher temperatures than the cold plate. As a result, heat flows through the specimen in the downward uniaxial direction within the region of the heater plate.

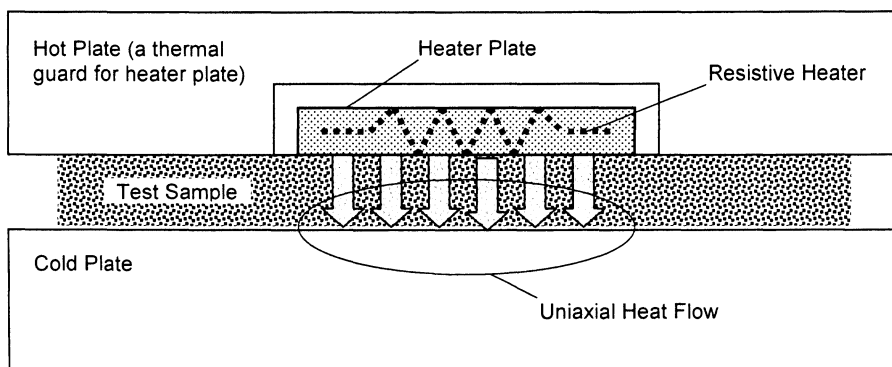


Figure 1.1: General outline of GHP apparatus

The thermal conductivity can be determined on the basis of Fourier's Law, considering the measured and known uniaxial heat flux, the specimen thickness, and the contact surface temperatures [9-11]. Overview on the design, operation and measurement principles of the GHP apparatus at the Thermofluids Research Laboratory at Ryerson University are described in a subsequent chapter.

1.2 Literature Review

1.2.1 Experimental Studies of Soil Thermal Conductivity

The effective prediction of soil thermal performance is critical for numerous practical applications and, as already mentioned, there is a lack of comprehensive experimental research, especially for cases of low moisture contents and high temperatures. To the author's knowledge, even the most recent and advanced analytical and numerical studies involving the theoretical modeling of soil thermal conductivity (amongst them Shiozawa and Campbell [2], Gori and Corasaniti [3], Pourhashemi *et al.* [4], Tarnawski and Leong [12], Tarnawski and Gori [13], Abu-Hamdeh [14], Naidu and Singh [15]) have been verified on the basis of limited experimental data, especially at temperatures beyond 60°C.

Sepaskhah and Boersma [16] measured the thermal conductivity of loamy sand, loam, and silty clay loam textures at two moderate temperatures of 25°C and 45°C using the heated probe method. In their experimental methodology, soil specimens were first dried by hot air and then packed into glass containers, so

each container comprised an equal amount of dry soil. In order to avoid air gaps, the soil was added in layers and hard-packed after addition of each new layer. In order to get the desired moisture content, the water was added during packing between the layers. The containers were closed and sealed using a scotch tape. To achieve a uniform moisture distribution all containers were kept in a constant temperature cabinet for several weeks prior to measurement. Regarding the experimental results, it is important to note that some presented data on soil texture, porosity, and bulk density data are incorrect or misprinted. In particular, the porosity and dry bulk density, provided for the loam and silty clay loam textures, result in unreasonably high densities for soils. Meanwhile the porosity for the loamy sand is misprinted.

Thermal conductivity measurements published by Campbell *et al.* [1] involved nine soils, covering three textural groups: coarse soils (L-soil, Royal, Volkmar), medium soils (Palouse-A, Salkum, Mokins, Walla Walla), and fine soils (Palouse-B, Boulder creek). In the experimental methodology, all samples were passed through a 2-mm sieve and then air-dried. Distilled water was added to obtain the desired moisture content; the samples were then mixed and packed into a pipe to a uniform bulk density. The plastic pipe was covered with cellophane and sealed with scotch-tape, then kept in a constant temperature oven to achieve a uniform moisture distribution. The heated probe method was employed to measure the thermal conductivity, involving a probe of 40 mm long and 0.9 mm in diameter with a temperature range from 30°C to 90°C at 20°C intervals. The experimental

results are valid only for the lower temperatures of 30°C and 50°C; for the 70°C and 90°C, the results vary randomly with moisture content.

The thermal study conducted by Black *et al.* [18] for Ottawa sand was based on heated dual-probe technique as well as a GHP apparatus. However the study does not mention the temperature range over which the measurements were taken. Moreover, the thermal conductivity measurements for the low moisture contents are significantly scattered and thus are of doubtful validity. The reason is probably moisture migration around the probes, which also resulted in the thermal conductivity measured by heated probe being on average lower than the GHP measurements.

A useful study was conducted recently on the basis of dual-heated probes by Kasubuchi and Hiraiwa [19] and involved the thermal conductivity measurement of clay loam and light clay soil textures for the temperature range of 5°C to 75°C, at 10°C intervals. The samples were carefully prepared first by hot air-drying and passing through a 2-mm sieve, and then the distilled water was added to get a required moisture content. After the addition of water the samples were mixed in the plastic bags and then packed in sample containers. The containers were heated in cycles in a microwave oven, then sealed with a hard plastic and silicon sealant, and finally left in a constant temperature environment to achieve a uniform moisture distribution. The experimental apparatus consisted of dual-heat probes made of stainless-steel needles, 50 mm in length with outer and inner diameters of 1 mm and 0.5 mm, respectively. The measurements were repeated for the same samples for verification and then averaged. Although the experiments seem to be

well conducted and the data are reasonable, the major limitation is the temperature range not being extensive enough for a comprehensive verification of either high (up to 100°C) or low (sub-zero) temperature models.

A common deficiency in all these studies is the absence of detailed information regarding particle size distribution and textural data of soil samples, which is crucial for refining an analytical model of thermal conductivity. The experiments are done over limited low- to mid-temperature ranges, in many cases exhibiting a questionable accuracy. Despite these limitations these datasets are commonly used for theoretical and numerical modeling.

1.2.2 Modeling of Thermal Conductivity of Soils

Numerous attempts have been made to model thermal conductivity. In general, the models can be classified as empirical or theoretical. The theoretical modeling involves an approximate analytical reconstruction of the actual soil structure, based on its properties, and as such is very challenging due to the dependence on a wide variety of parameters, including mineral composition of soil particles, particle shape and size distribution, temperature, dry density, porosity, water content, etc. Some of these parameters are hard to measure precisely, and it is difficult to incorporate all of them into a single universal model [20, 21]. Moreover, analytical models normally involve empirical coefficients which also can not be estimated precisely [21]. In comparison, the empirical modeling is based purely on the numerical and mathematical analysis of experimental data. Empirical

correlations are much easier to use and incorporate in numerical algorithms, but are primarily dependent on the accuracy of the experimental data [22].

Numerous correlations for soil thermal conductivity have been proposed in the literature. Among others, Kersten [23], Gemant [24], Johansen [25], De Vries [26], Van Rooyen and Winterkorn [27], Cote and Konrad [5], Tarnawski and Leong [12], and Tarnawski and Gori [13] have developed correlations that vary in complexity. Each of these correlations is limited to a certain type of soil as well as specific conditions, as surveyed and reviewed by Farouki [28].

Kersten [23] based his correlations on the empirical data he collected. He produced equations for the thermal conductivity of frozen and unfrozen silt and sandy soils as a function of moisture content and dry density. However, as shown by Farouki [28], Kersten's correlation is accurate only for the frozen soils with saturations up to 90%. Also, for very low degree of saturation down to dry state, it produces negative thermal conductivity values.

Gemant's correlation [24] assumes an idealized geometrical model of soil particles with point contacts. The soil thermal conductivity is derived as a function of dry bulk density (ratio of dry soil mass to dry soil volume), moisture content, apex water (i.e. water collected around the contact points), water absorbed as a film around the soil particles, and thermal conductivities of water and solids. However, Gemant's correlation gives a reasonable estimate for only unfrozen sandy soils.

Johansen's correlation [25] presents the soil thermal conductivity as a function of the degree of saturation, and is suitable for both coarse and fine

grained soils in the frozen and unfrozen states. However, the accurate results are limited to moisture contents up to 20%.

The De Vries correlation [26] based on the assumption that soil is comprised of two phases, considering solid uniform ellipsoidal particles within fluid. The method represents the thermal conductivity as a function of the solid volume fraction and the thermal conductivities of the solid and fluid phases. However its results are reasonable only for unfrozen coarse soils with saturations from 10% to 20%.

The correlation developed by Van Rooyen and Winterkorn [27] is based on data collected from sands and gravels. The thermal conductivity is given as a function of the degree of saturation, dry density, mineral type, and particle shape. The Van Rooyen and Winterkorn correlation is limited to unfrozen sands and gravels with saturation levels between 1.5% and 10% only.

A common deficiency in all these correlations is that they are commonly limited to a single soil type, or a very narrow range of moisture contents. Thus none of the above correlations can be universally incorporated into numerical heat transfer algorithms.

1.3 Objectives and Scope of Research and Applications of Results

The prime objective of this research is to aid the development of accurate analytical as well as empirical high-temperature models of soil thermal conductivity by establishing comprehensive sets of experimental data over a wide temperature

range for two soils of different textures (Ottawa sand and Richmond Hill clay-loam) with established physical properties. The research is carried out using the guarded hot plate methodology. Among the factors that affect soil thermal conductivity, texture, temperature and moisture content, by far, have the greatest impact upon it [22, 29, 30]. In particular, in the experimental method employed, the soil thermal conductivity is measured for temperature variation from 2 to 92°C, at 10 °C intervals, and moisture content variation from complete dryness to full saturation with a targeted measurement error of less than 3%, which, to the author's knowledge, is not yet available in the literature. One of the primary applications of the gathered data will be to verify existing analytical models of soil thermal conductivity. Consequently, the models could be recalibrated and modified to improve their accuracy.

As a second part of the project, accurate empirical correlations for soil thermal conductivity as a function of moisture content and temperatures are developed for the experimental soil types based on the gathered datasets. The developed correlations could be easily incorporated in numerical algorithms within any simulation software package that deals with heat transmission through soils, such as the ESP-r or EnergyPlus for building energy simulations.

1.4 Outline of the Thesis

The remainder of the thesis is comprised of the following sections. First, an overview of the modified guarded hot plate apparatus and data acquisition system

(on the basis of which the experiments are conducted) is provided. Then, an extensive numerical analysis of heat transfer within the GHP apparatus is conducted to check and validate the initial design and later modifications. After, the experimental methodology and soil specimen preparation techniques are described in detail. Then, the experimental results are presented, analyzed, and verified. Based on gathered datasets, empirical correlations for the types of soil involved are developed. To illustrate the importance of the effective soil thermal conductivity for underground heat transfer problems and also to illustrate the application of developed correlations, a numerical simulation of heat loss from a basement surrounded by Ottawa sand and Richmond Hill clay-loam is performed. Finally, the research is summarized and recommendations are made.

CHAPTER**2****AN OVERVIEW OF RYERSON GUARDED HOT PLATE APPARATUS**

2.1 Introduction

This chapter describes the operational principles and construction of the guarded hot plate apparatus. First, a general overview of the experimental apparatus is presented to familiarize the reader with its major parts and components. On this basis, the measuring technique for thermal conductivity is introduced. Consequently, the construction, design modifications, as well as operation and calibration methodologies are described in detail. An extensive review of GHP fundamentals and an analysis of various GHP measurement techniques are given in references [10, 11, 31].

2.2 Overview of GHP Operation Principles

The guarded hot plate methodology is a steady-state technique based on the precise monitoring of steady heat flux flowing through a specimen between the planes of hot and cold plates (refer to Figure 2.1 for a schematic layout of apparatus). A hot plate acts as a thermal guard for the heater plate embedded into

it. Both hot and heater plates are maintained at the same temperature ($T_h \approx T_{hr}$), however they are independently heated by a heat transfer fluid and by an electrical heater, respectively, and thus are separated by a small air gap to minimize heat flows during temperature balancing, except where a heat flux meter is placed. In turn, the cold plate is maintained at a lower temperature to create a downward heat flow through the specimen between the plates. It is important to note that since the heater plate is surrounded by the hot plate at the same temperature, in the region underneath it the heat flux through the specimen is linear and downward unidirectional, creating uniform isothermal planes across the specimen in that area. Thus, the experimental specimen area is defined as a square contained within the air gap centerline between the front faces of hot and heater plates.

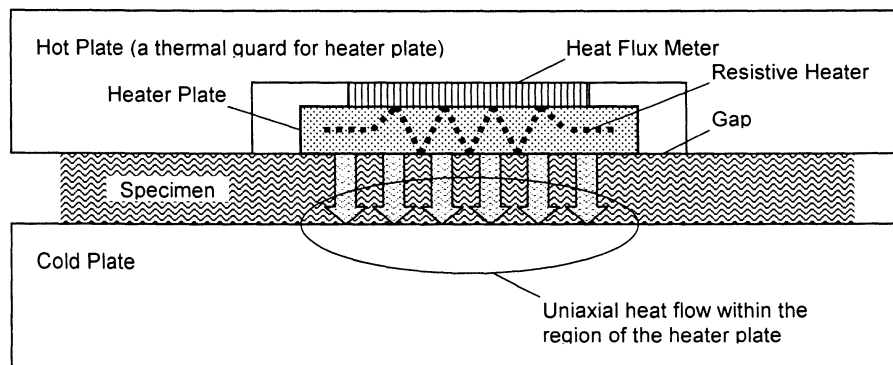


Figure 2.1: General schematic of a GHP apparatus.

The thermopile heat flux meter is placed between the heater plate and the hot plate to measure the heat transfer between them during temperature balancing. When the temperatures of the hot and heater plates are balanced, the heat transfer between them is negligible, which is indicated by a zero *emf* output of the

heat flux meter.

2.2.1 Measurement of Thermal Conductivity

The measurement of thermal conductivity is based on Fourier's law for conductive heat transport:

$$q = \lambda A \left(\frac{\Delta T}{L} \right) = \lambda A \left(\frac{T_{hr} - T_c}{L} \right) \quad (2.1)$$

where q is the rate of thermal energy flow through the specimen, λ is the thermal conductivity, A is the experimental cross-sectional area of the specimen (being a surface area of the heater plate), ΔT is the temperature difference between the heater, T_{hr} , and cold, T_c , plates, and L is the uniform thickness of the specimen.

Consequently, the general expression for the thermal conductivity becomes:

$$\lambda = \frac{q}{A} \left(\frac{L}{T_{hr} - T_c} \right) = q'' \left(\frac{L}{T_{hr} - T_c} \right) \quad (2.2)$$

where q'' is the rate of thermal energy flow through the specimen per unit area, or in other words heat flux. The heat flux could be measured directly on the basis of hybrid methodology which comprises two concepts: a primary measurement method based on the first law of thermodynamics, and a secondary method based on the Newton's law of cooling [32]. To illustrate the hybrid method, let us consider the assembly of the hot plate, the heater plate, and the heat flux meter, shown in Figure 2.2.

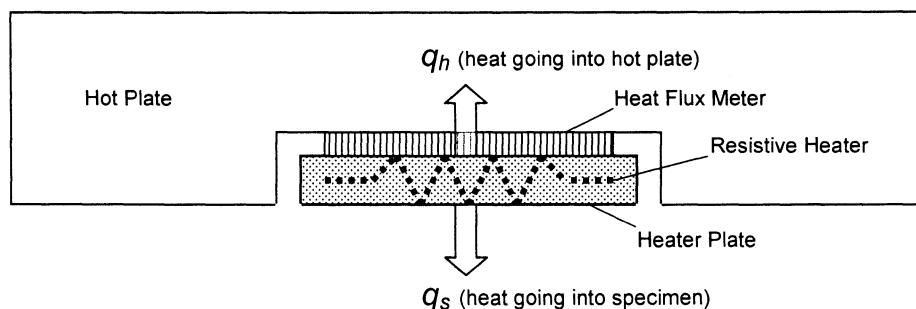


Figure 2.2: Assembly of hot plate, heater plate, and heat flux meter.

The heat transfer rate of interest is obviously the one going into the specimen, and is determined as follows, assuming a steady-state heat balance:

$$q_s = q_e - q_h \quad (2.3)$$

where q_s is the heat transfer rate going into the soil sample, q_e is the power supplied to the electrical heater inside the heater plate by a programmable power supply, and q_h is the heat transfer rate going into the hot plate, passing primarily through the heat flux meter whose *emf* output is directly proportional to the temperature difference across it. By definition, the electrical power is given by:

$$q_e = V \cdot I \quad (2.4)$$

where V is the voltage across and I is the current through the electrical resistance inside the heater plate.

Although the heater plate temperature should be adjusted to exactly equal the hot plate temperature, in reality they may slightly differ, resulting in a heat transfer going from/into the hot plate which has to be accounted for, namely:

$$q_h = \alpha \cdot e \quad (2.5)$$

where e is the *emf* output of the heat flux meter, and α is a proportionality calibration constant (refer to Section 2.4 for details). This is in fact an interpretation of the Newton's law of cooling, where *emf* is proportional to the temperature difference between the heater and hot plates, δT . Moreover, since the heater plate and the hot plate are both assumed to be isothermal, the *emf* output should be proportional to q_h even though the heat flux meter is in direct contact with only a portion of the back surface of the heater plate, and hence:

$$q_h \propto emf \quad (2.6)$$

with q_h accounting for the total heat transfer from/into the hot plate, including the transfer through fasteners and electrical wires, that are heat-sinked to the hot plate. Finally, by combining Equations (2.2), (2.3), (2.4), and (2.5), the expression for the thermal conductivity of the specimen becomes:

$$\lambda = \frac{VI - \alpha e}{A \left(\frac{T_{hr} - T_c}{L} \right)} \quad (2.7)$$

However, in actual situation, the soil specimen is contained inside a container, and a silicon rubber pad is placed on each side of the container (see Section 3.1 for details). Therefore taking into account the thermal resistances due to container walls and silicon rubber pads, the thermal conductivity of the specimen is then obtained as:

$$\lambda = \frac{L_S}{A \left(\frac{T_{hw} - T_c}{VI - \alpha e} \right) - \frac{L_{SR}}{\lambda_{SR}} - \frac{L_{CW}}{\lambda_{CW}}} \quad (2.8)$$

Where L_S , L_{SR} , and L_{CW} are the thicknesses of soil specimen, silicon rubber pads, and electroplated steel container walls, respectively; λ_{SR} and λ_{CW} are the thermal conductivities of silicone rubber and electroplated steel, respectively.

2.3 Overview of Modified GHP Apparatus

The modified Ryerson GHP single specimen apparatus is shown in Figure 2.3 below, and is comprised of hot and cold plates installed on a rotating self-leveling frame (Figure 2.4). The frame allows adjusting the position angle of the plates from horizontal to vertical (note that throughout the experiment the plates are always fixed horizontally, with the hot plate being on top of the cold plate, to prevent any natural convection), with a maximum possible specimen thickness of 38 mm. The hot and the cold plates are each heated independently by a heat transfer fluid that is pumped through a series of channels inside each plate; the cold and hot heat transfer fluids are maintained at constant temperatures by two programmable circulating baths, one for each plate; both baths are upgraded with thermoelectric coolers placing over fluid reservoirs to condense the vapour of heat transfer fluids at high temperatures and minimize evaporation losses. Meanwhile the heater plate, embedded into the hot plate, comprises an electric heater and is powered by an external programmable power supply. All equipment and special materials that were implemented are specified in the inventory list (Table 2.1).

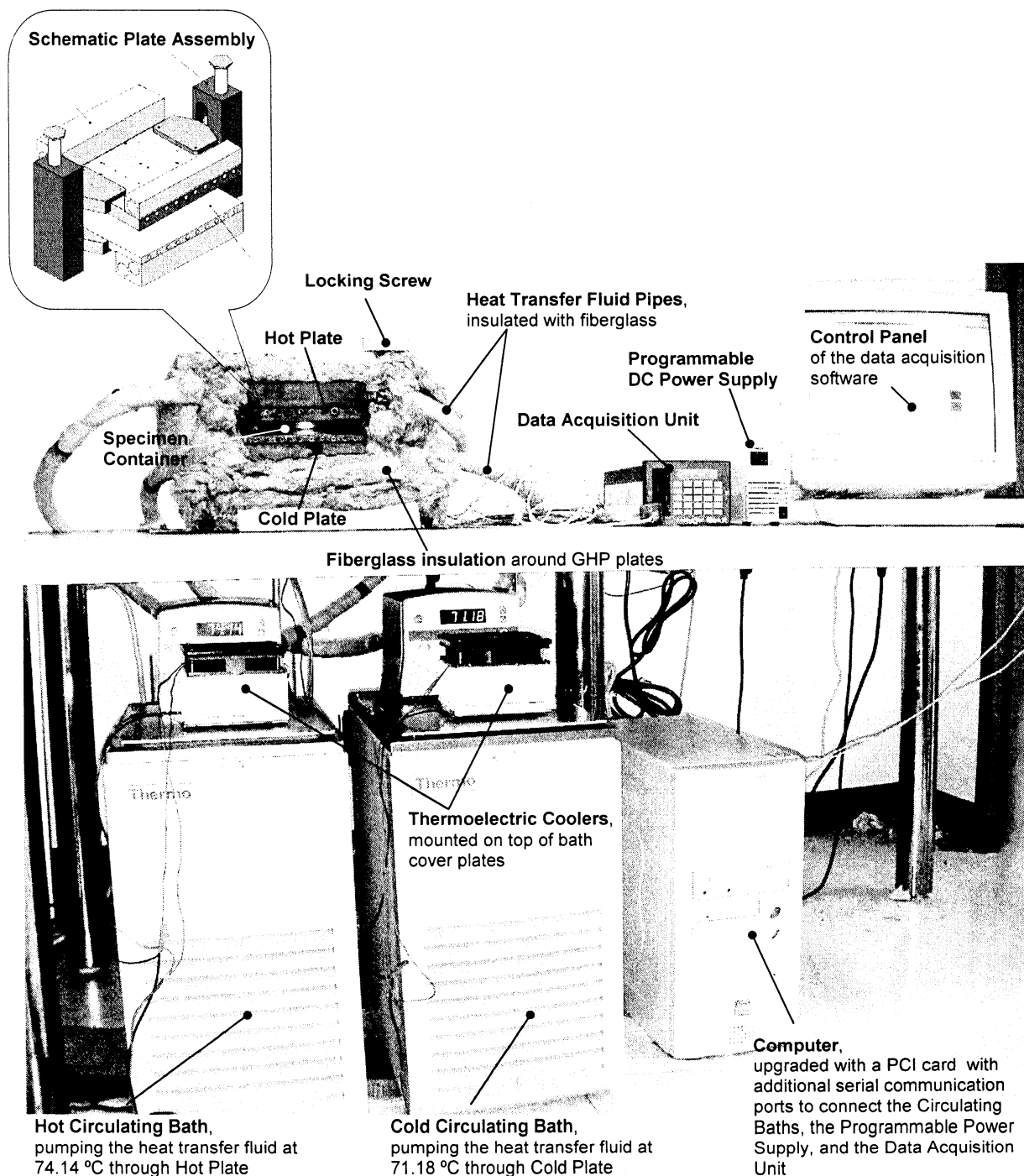


Figure 2.3: The Ryerson GHP apparatus.

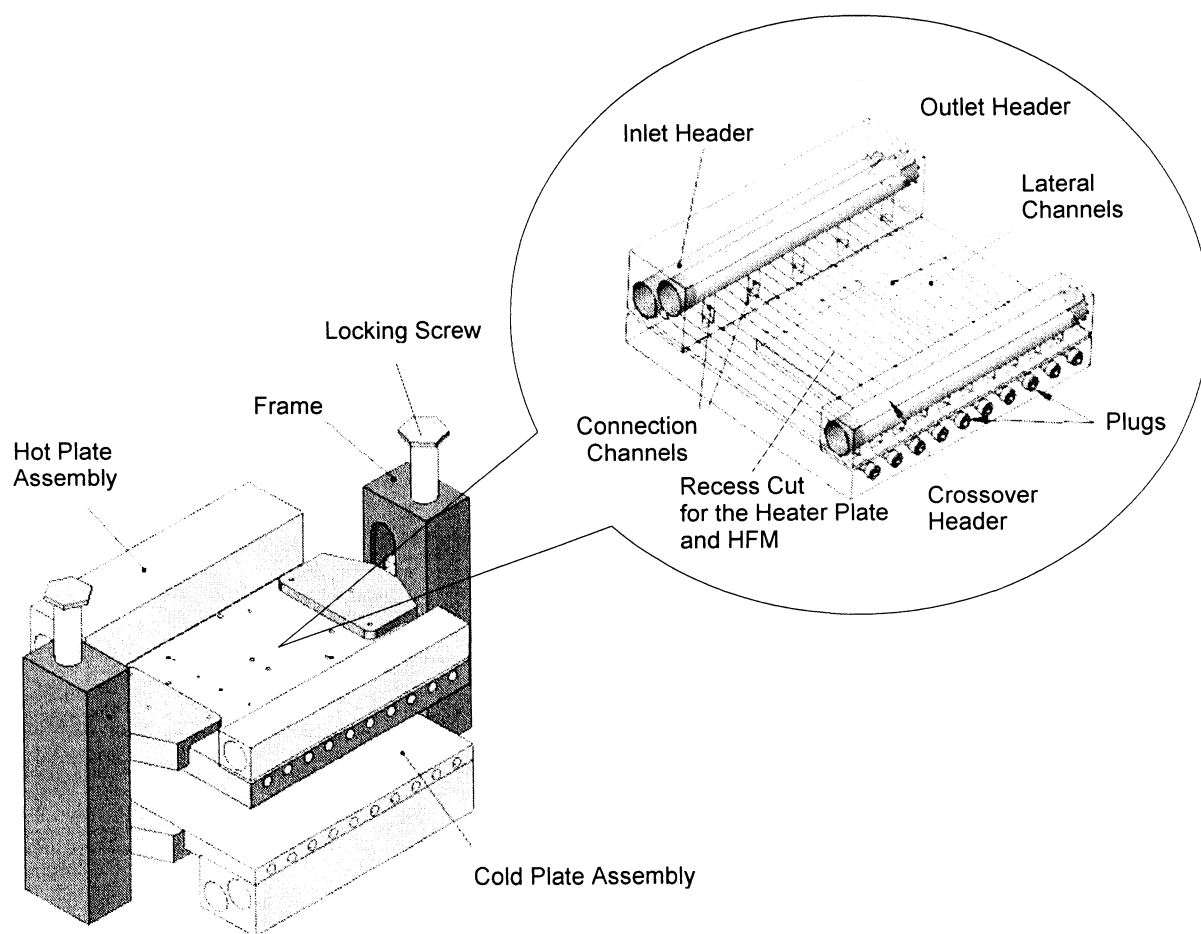


Figure 2.4: Schematic of GHP plate assembly (hot plate is shown without the heater plate and heat flux meter) [11].

Table 2. 1: GHP apparatus inventory list.

Description	Manufacturer	Model	General Specifications
A PCI card	Connect Tech Inc.	Blue-heat/PCI RS-232/485	4 serial port model
Two thermoelectric coolers	Custom made		50 W
Two circulating baths	Thermo Electron Corporation	Neslab RTE 740 Digital Plus	Bath volume: 7.2 L Temp. Range: -40°C to +200°C Temp stability $\pm 0.01^\circ\text{C}$ Pump capacity: up to 15 Lpm at 0 head
A data acquisition unit	Daytronic Inc.	System 10 Model 10A65-8 with 8-channel low-level analog card	<p><u>$\pm 50\text{mV}$ Range:</u> Resolution=$24\mu\text{V}$, Bias error=0.02%, Precision error=$100\mu\text{V}$.</p> <p><u>$\pm 100\text{mV}$ Range:</u> Resolution=$49\mu\text{V}$, Bias error=0.02%, Precision error=$100\mu\text{V}$.</p> <p><u>$\pm 200\text{mV}$ Range:</u> Resolution=$98\mu\text{V}$, Bias error=0.02%, Precision error=$100\mu\text{V}$.</p>
A programmable DC power supply	Nemic-Lambda Ltd.	Zero-UP 10-20	<p><u>For constant voltage:</u> Range: 0 to 10 V with 2.8 mV resolution. Stability: $\pm 0.01\% + 2 \text{ mV}$ (at ambient temp. $20^\circ\text{C} \pm 5^\circ\text{C}$)</p> <p><u>For constant current:</u> Range: 0 to 20 A with 6 mA resolution. Stability: $\pm 0.02\% + 5 \text{ mA}$ (at ambient temp $20^\circ\text{C} \pm 5^\circ\text{C}$)</p>

A 1mA current source	Custom made	Standard 1mA	Stability $\pm 0.0015\text{mA}$ (at ambient temp. $20\pm 5^\circ\text{C}$)
A heat flux meter	TNO Institute of Applied Physics, Netherlands	60mm x 3mm disk with 800 embedded thermocouples	<i>Emf</i> (at 20°C): $\sim 1\text{mV}$ per 4.78 W per m^2 of HFM area HFM thermal resistance (at 20°C): $\sim 4.25\text{ K/W}$ Sensitivity (at 20°C): $\sim 25\text{ mV/K}$ Accuracy of calibration value: 5% Maximum temp.: 250°C
Two platinum resistance temperature detectors (RTD)	Omega Corp.	Omegafilm RTD, Series F	Dimensions: $2.3 \times 2 \times 1\text{ mm}$ Nominal resistance: 100Ω at 0°C Repeatability: 0.010°C
A platinum resistance thermometer (PRT)	Azonix Corporation	Model 12001A-1262A	Repeatability plus accuracy: 0.006°C
Ten Cu/Cn thermocouples	Custom made	36-gauge Cu and Cn wires	Cu/Cn sensitivity: $40\ \mu\text{V/K}$ Temp. difference resolution: $\pm 0.025^\circ\text{C}$
Heat transfer fluid	Petro Canada	CalFLO LT	Operating temp. range: -30°C to 250°C

2.3.1 Plate Assembly

All plates were made of 99.8% pure copper to achieve an isothermal condition, which is required for the hybrid method. The hot and cold plates are 178×178×19 mm, and mounted with inlet/outlet and crossover headers to connect a series of ten internal flow passages of 6.35 mm in diameter through each plate (refer to Figure 2.4). The headers and flow passages form a reverse flow arrangement system of forward and return flow within a bank of five inlet laterals and five outlet laterals, respectively. As the heat transfer fluid flows through the system, it first enters the inlet header of 18.3 mm in diameter and from there flows through five inlet laterals into the crossover header, where it is reversed and forced through five outlet laterals into the outlet header. The inlet and outlet laterals alternate to achieve a uniform temperature distribution along an entire plate within a maximum of 0.01°C difference between the first and last lateral, considering the maximum operational temperature of 200°C, the temperature difference of 10°C between the hot and cold plates, and an average heat flux of 1675 W/m² across the plates [11]. To measure the temperature difference between the surfaces of hot and cold plates, a Cu/Cn thermopile was employed. The thermopile was assembled of five thermocouple pairs, each made from the 36-gauge Cu and Cn wires by soldering their junctions. The thermocouple junctions were then embedded into the hot and cold plates at the locations shown in Figure 2.5, and connected in series. To measure the actual surface temperatures of the hot and cold plates, two platinum resistance temperature detectors (RTD) were embedded into the

plates as shown in Figure 2.5. The RTDs were connected in series to a standard 1mA current source, and have an overall bias error of $\pm 0.030^{\circ}\text{C}$.

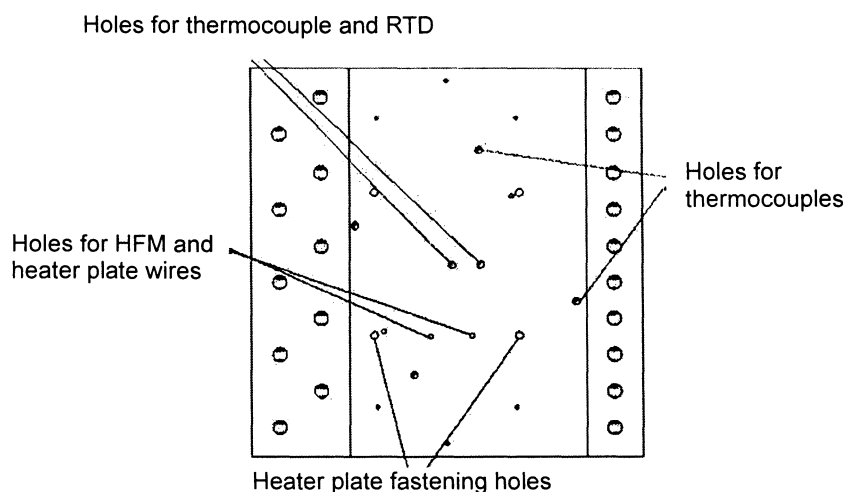


Figure 2.5: Positions of thermocouples, thermopile, and RTD on the hot plate (top view) [11].

The heater plate is installed in a $77.8 \times 77.8 \times 6.4$ mm recess in the center of the hot plate which is shown in Figure 2.4. The heater plate is 76.2×76.2 mm and 3.28 mm thick and has a nominal heat transfer measurement area of 0.00581 m^2 . The heater plate is assembled of two copper plates. One of the plates has a 3.18×1.59 mm serpentine groove with 18.4 mm spacing machined in it as shown in Figure 2.6 below (the detail engineering drawings and dimensions of all plates as well as other components of GHP apparatus are provided in [11]). A 26-gauge nichrome wire with an approximate resistance of 1.5Ω is placed in the groove and electrically insulated with ceramic paste, and the plates are soldered together with the wire in between them. The edge of the plate is chamfered to a 45° angle to minimize the heat transfer from the side of the plate.

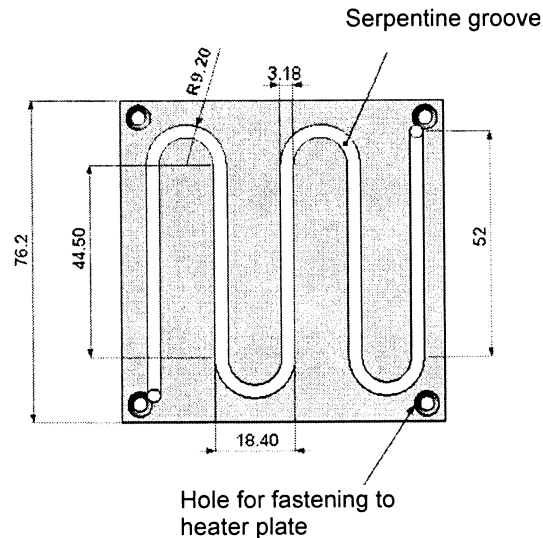


Figure 2.6: Heater plate with a serpentine groove for nichrome wire. All dimensions are in mm [11].

In order to measure the heat transfer between the heater plate and the hot plate, a heat flux meter is placed between them, as shown in Figure 2.7. The heat flux meter is a silicone rubber disc 60.0 mm in diameter, 3.0 mm thick, with about 800 embedded thermocouples forming a thermopile, and has an approximate thermal resistance of 4.25 KW.

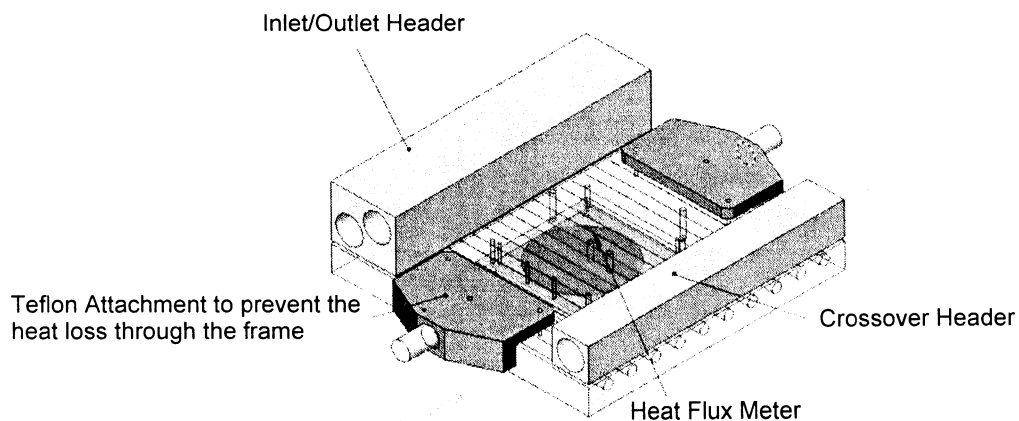


Figure 2.7: A complete assembly of the hot plate, the heater plate, and the heat flux meter in between [11].

The assembled plates were mounted on the self-leveling supporting frame through Teflon attachments that minimize heat transfer from/into the frame. The inlet/outlet headers of hot and cold plates were then connected to the hot and cold circulating baths using flexible stainless steel pipes. Finally, the plate assembly and the heat transfer fluid lines were well insulated with fiberglass, as shown in Figure 2.3.

To test and validate the overall design and experimental setup of the guarded hot plate apparatus, an extensive numerical heat transfer simulation for a complete plate assembly with a specimen has been performed (refer to Chapter 3). The simulated temperature variations over the surfaces of the heater, hot, and cold plates proved to be insignificant. In particular, a conservative estimate of the temperature variations over these plates for a possible maximum experimental temperature of 200°C and temperature difference of 10°C did not exceed 0.025°C.

2.3.2 Automated Operation of GHP Apparatus

The computer was upgraded with a Blue-Heat RS-232/485 PCI card manufactured by Connect Tech Inc. with four additional serial communication ports in order to connect the hot and cold circulating baths, the programmable power supply and the data acquisition unit. A data acquisition software *GHP Control v.2.0* was specially developed using Visual Basic to synchronize and control these components, completely automating the experimental procedures,

as well as data collection and analysis. The general block diagram of the code is presented in Figure 2.8 (the initial version of the code was developed by Reid [11], and was significantly modified and improved throughout this project). The program consists of the following stages. First, the initial data, which includes thickness of the specimen, initial and final experimental temperatures, the temperature difference between the cold and the hot plates, and the temperature increment, are entered into a control panel of the data acquisition software. Then, the circulating baths are powered on and set to specified temperatures, and the system is allowed to stabilize, which takes about 40 minutes. After the hot and cold plates stabilize, the heater plate temperature starts to be balanced and eventually matched to the constant temperature of the hot plate. This is done by adjusting the electrical power supplied by a programmable power supply to the heater plate until the *emf* output of the heat flux meter read by a data acquisition unit becomes practically zero. Typically, the hot and heater plate temperatures are within 0.01°C difference, as indicated by the *emf* output of the heat flux meter. It is also important to note that even though the 0.01°C difference is insignificant in comparison to the 2-5°C difference between the hot and cold plates, the possible back heat flow (q_h) between the hot and heater plates is still measured and accounted for (Equation (2.3)). The *emf* resulting from the temperature difference between the heater plate and the hot plate is used as a feedback sensor in a balancing loop to achieve a right amount of electrical power supply to the heater plate, which is based on a *high-low control* technique. The technique involves continuously narrowing the voltage range (until less than 5

mV, which is close to the power supply resolution of 2.8 mV) in which lies the power output required to achieve an *emf* close to zero. In particular, the high and low output powers are alternated according to the following: when the *emf output* of the HFM is negative (indicating that $T_{\text{htr}} < T_{\text{h}}$), the power is increased to the high power. On the contrary, when the *emf* is positive (indicating that $T_{\text{htr}} > T_{\text{h}}$) the power is decreased to the low power. Meanwhile, the time periods, Δt_i , of power being set at high or low are also recorded. It has been observed that 13 alternations are statistically enough to estimate a new power setting, P_{est} , using:

$$P_{\text{est}} = \frac{\sum_{i=4}^{13} P_i \Delta t_i}{\sum_{i=4}^{13} \Delta t_i} \quad [2.9]$$

The new estimated power is then set. Subsequently the new high and low output powers are set by reducing the initial voltage range by half with the new estimated power being the midpoint, and the alternation process is repeated until the voltage range is less than 5 mV. Note that for the calculation of the power estimate (Equation (2.9)) the first three alternations are disregarded due to unrepresentative amounts of time required for the power supply to initially adjust the heater plate from the initial arbitrary state. Finally, when the temperature balance between the heater and hot plates is achieved, the system is paused for 5 minutes to ensure a steady state, and then the data acquisition begins. The above-described high-low control technique is an improved and refined version of the one originally used by Reid [11]. As a result, the technique is more effective in terms of accuracy and time. A total of 200 measurements of *emf* from the HFM, power to the heater plate, temperatures of the hot and cold plates, and the

temperature difference between them are recorded over a period of about seven minutes. It has been observed that the precision index of the mean (due to the 200 measurements) of each parameter is relatively insignificant comparing to its bias error. Based on the mean values of the parameters, the thermal conductivity is calculated (refer to Equation (2.8)), taking into account the effects of sample container and two silicone rubber pads (which are sandwiched between the sample container and the plates, as discussed in Chapter 3). One experimental measurement is now completed, and the temperature is raised according to the specified increment and the entire process is repeated so as to find the thermal conductivity value for a new temperature setting.

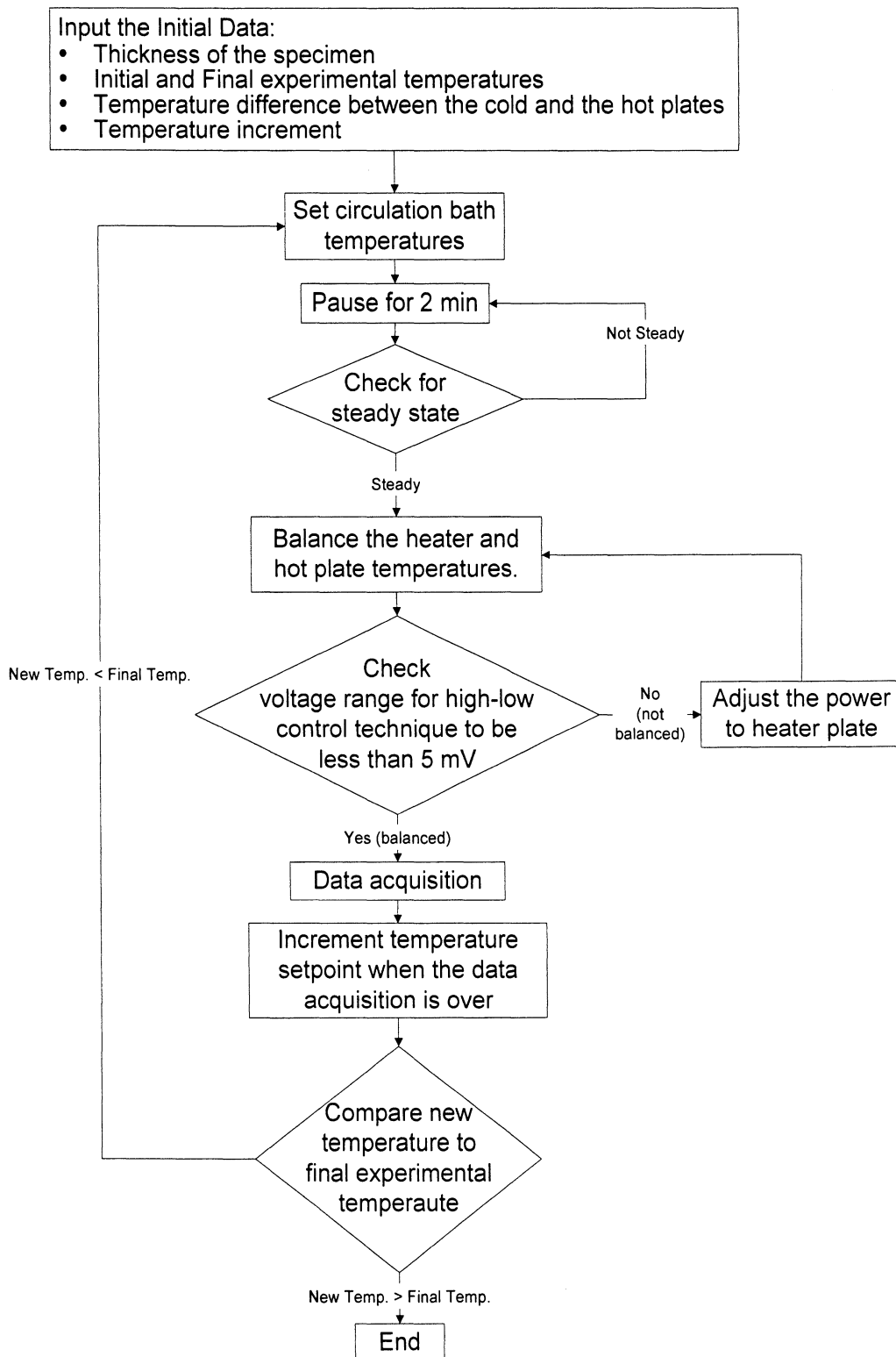


Figure 2.8: Block diagram of *GHP Control v.2.0* data acquisition software.

2.4 Calibration of GHP Apparatus

Before the experiment can commence, all sensors and measuring devices of GHP apparatus had to be recalibrated with respect to the maximum equipment temperature range from 0 to 200°C. This is comprised of several stages, in particular: a) calibration of the heat flux meter, b) calibration of RTDs embedded in the plates, and c) calibration of internal RTDs of the hot and cold circulating baths. All the calibrations were done in situ and followed the calibration methodology outlined by Reid [11]. The calibrations of the heat flux meter and the RTDs embedded in the plates were performed very carefully over considerable amount of time, in order to ensure the accuracy of the apparatus.

2.5 Experimental Error Analysis

The overall error of each measurement is a combination of errors from various sources, such as non-uniformity, calibration, signal conditioning, data acquisition and data reduction. The overall uncertainty associated with the 95% confidence level $U_{0.95}$ of thermal conductivity λ is obtained using the root-sum-square (RSS) method [33]. Conservative estimates of all measurement errors and $U_{0.95}$ of λ by Reid [11] are summarized and listed in Table 2.2. For a typical ΔT of 4°C, the overall bias errors for temperature difference ΔT and mean temperature T_m are 0.064°C and 0.045°C, respectively, and the $U_{0.95}$ for λ is 2.67%. Detailed descriptions of the error analysis methodology and calculations can be obtained in [11].

Table 2.2: Overall bias errors of measured quantities and $U_{0.95}$ of λ [31]

Quantity	Overall bias error/ $U_{0.95}$
$\Delta T = T_h - T_c$	$\sqrt{3 \times 10^{-6} \Delta T^2 + 4 \times 10^{-3}}$ ($^{\circ}\text{C}$)
$T_m = (T_h + T_c)/2$	$\sqrt{3.3 \times 10^{-6} \Delta T^2 + 2 \times 10^{-3}}$ ($^{\circ}\text{C}$)
A_{hp}	2.1%
L	0.51%
q_e	0.036%
q''	2.1%
λ	$\sqrt{39 \Delta T^{-2} + 4.7}$ (%)

CHAPTER
3
NUMERICAL ANALYSIS OF THE GHP ASSEMBLY
WITH A SOIL SPECIMEN

3.1 Introduction to Numerical Model

Any numerical simulation involves the mathematical approximation of the actual physical problem by defining the governing equations and specifying the boundary conditions over the computational domain. The domain is then discretized into a number of sub-regions or elements. Consequently, the complex governing equations are reduced from non-linear partial differential equations over an entire continuous domain to a system of linear algebraic equations over each element of the discretized domain. The system of equations is then solved to obtain the temperatures at each node of each element. This chapter covers the development, validation and analysis of the numerical model of the GHP apparatus with a soil specimen.

A numerical heat transfer analysis was carried out using FEHT [34], a commercially available finite element software package. Since the geometry of the GHP apparatus is symmetrical about its vertical center planes YZ and YX (as shown in Figure 3.1), and the temperature field is designed to be uniform along

and across the entire surface areas of the hot, the heater and the cold plates, the numerical analysis could be done in 2-D instead of 3-D which is significantly less time-consuming in terms of model development as well as computation. The model was created to scale and involved exact specifications of the actual apparatus, comprising an entire insulated GHP assembly with electroplated steel container packed with specimen soil (refer to Figure 3.1). In order to minimize the contact resistance between the plates and the container, as well as to prevent thermal short-circuit between the hot and heater plates through the container, thin pads of silicone rubber are placed between the container and the plates. The pads were also included in the numerical model, and are shown in magnified view in Figure 3.2. Meanwhile, the heater plate is placed in the recess within the hot plate with its front face flush with the front face of the hot plate, and a heat flux meter is sandwiched between them.

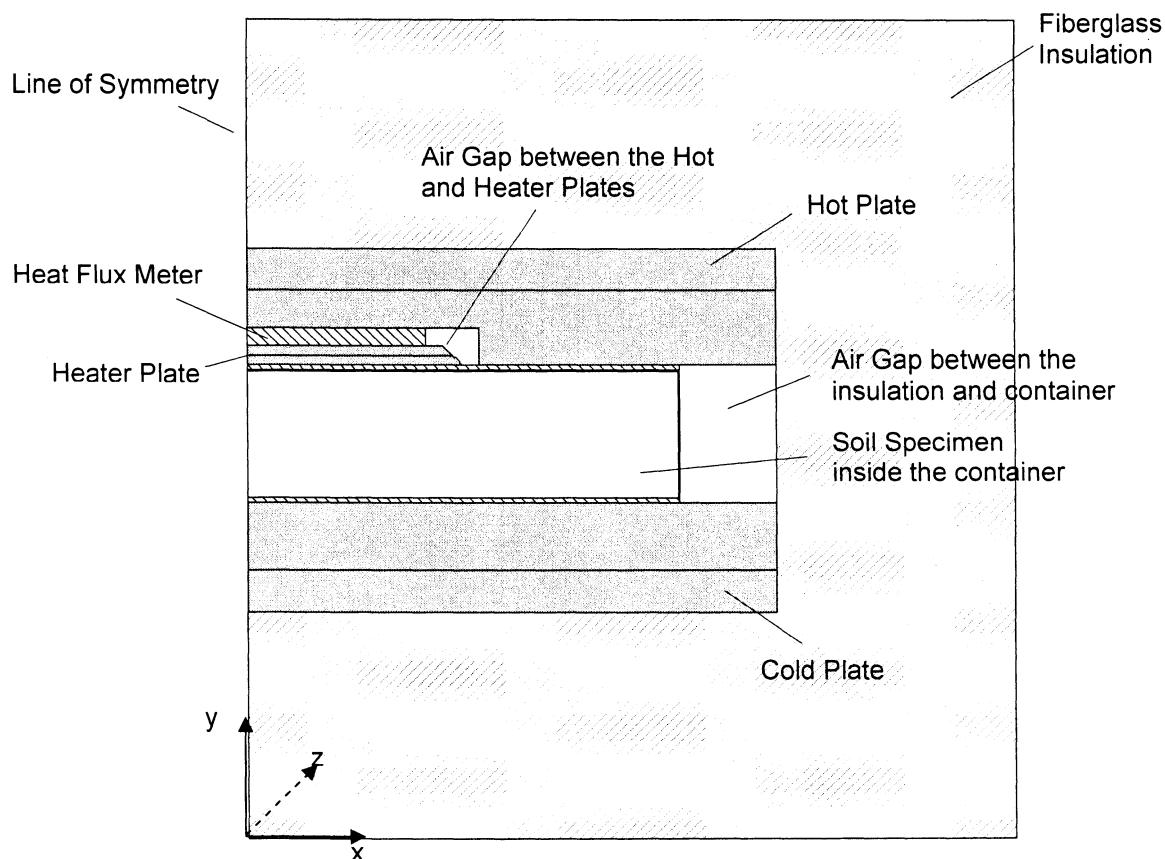


Figure 3.1: Model of a GHP assembly including a container with soil specimen.

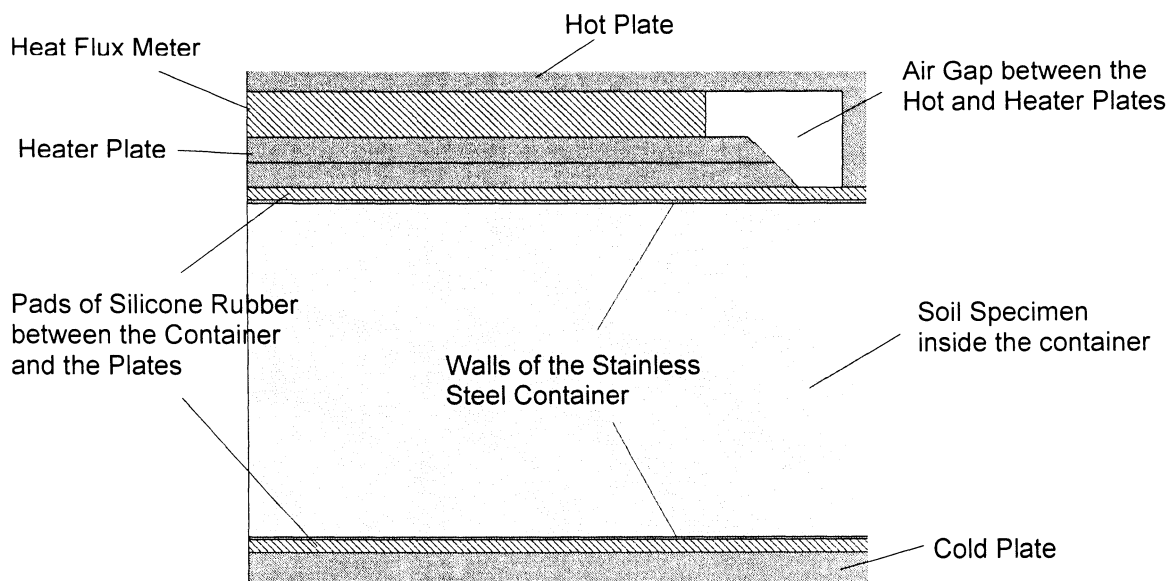


Figure 3.2: Magnified view of a portion of the model showing details about the silicone rubber pads, the steel container, the heat flux meter and copper plates.

For the simulation to be conservative, it was done at a maximum operational temperature of 200°C, thus involving the largest temperature gradients. Also, three temperature differences of 10, 5, and 2°C between the hot and the cold plates (typical experimental settings) were considered to study their effects on the temperature distribution pattern within the system. The properties of all materials involved in the numerical model are provided in Table 3.1. Note that a conservative estimate of soil thermal conductivity was chosen to be 2.50 W/m·K.

Table 3.1: Material properties used to model the components of the GHP assembly.

Component	Thermal Conductivity (W/mK)	Density (kg/m ³)
Soil specimen	2.5	2050
Electroplated steel	56	7854
Copper plates	401	8954
Silicone rubber pads	0.21	350
Fiberglass insulation	0.035	10
Air gaps	0.0259	1.177
HFM	0.25	350

3.2 Discretization of Computational Domain

The meshing (or discretization) has a tremendous impact on the solution of the numerical simulation in terms of its accuracy as well as the required computing resources. In this study the computational domain was discretized into linear triangular elements using the automatic meshing algorithm available in FEHT. The finite-element grid was then modified manually and made denser in

the regions where high temperature gradients were expected as well as in the areas of sudden geometrical changes where the boundaries were needed to be described in detail. The effect of element size was also tested and analyzed through a grid sensitivity study (Section 3.4) to ensure that the simulation results are consistent and independent of grid density. The final meshed domain is shown in Figure 3.3 and comprises 2882 nodes and 7628 elements, keeping the number of nodes to the minimum to save computing resources.

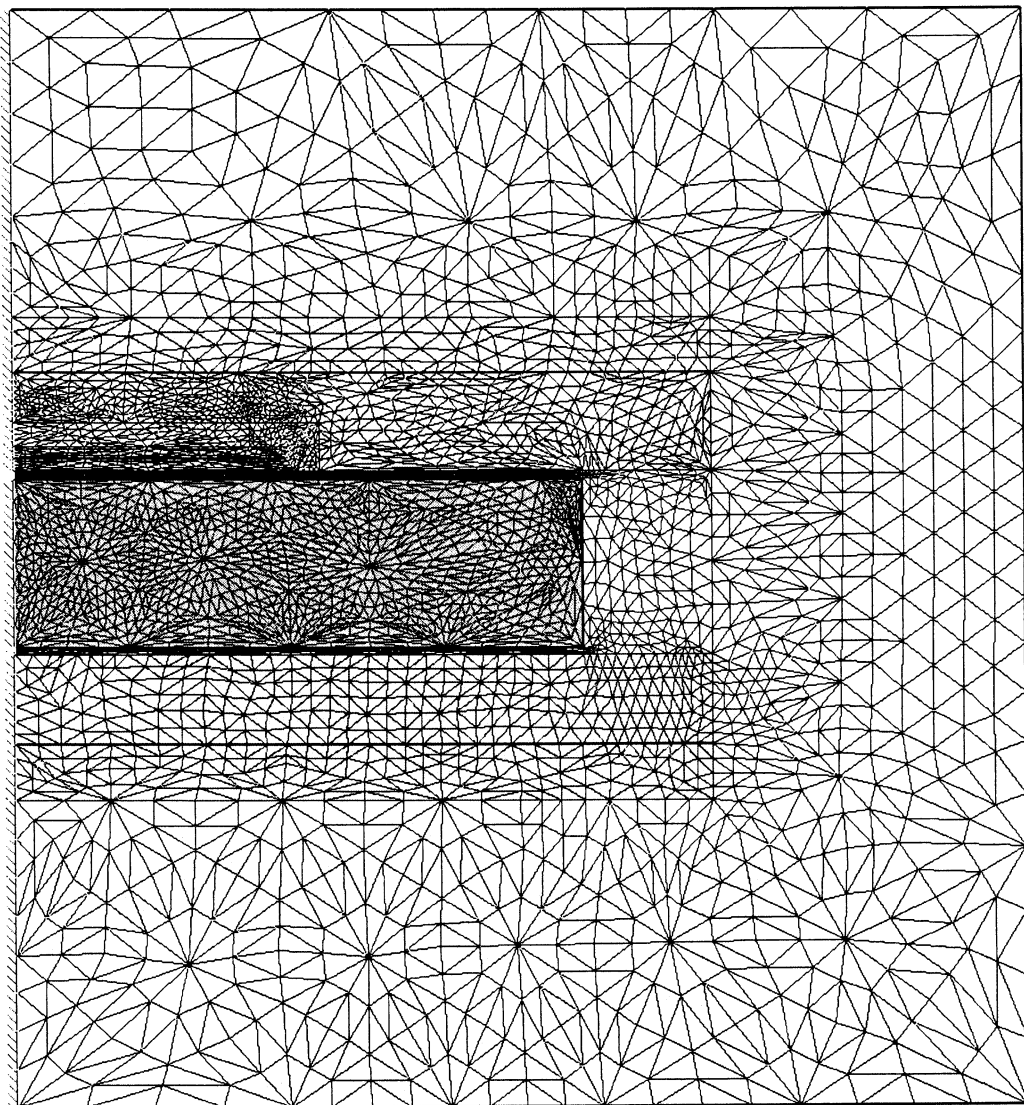


Figure 3.3: Discretized domain with 2882 nodes and 7628 elements.

3.3 Mathematical Formulation

The system is governed by Laplace's equation (3.1) in two dimensions. Laplace's equation is considered assuming steady state conditions, isotropic conductivity, and no heat storage or heat generation within the elements. The two-dimensional Laplace's equation is as follows:

$$\frac{\partial^2 T}{\partial x^2} + \frac{\partial^2 T}{\partial y^2} = 0 \quad (3.1)$$

3.3.1 Boundary Conditions

Listed below are the boundary conditions for the computational domain shown in Figure 3.4:

1. The Neumann adiabatic condition is applied to the line of symmetry OS:

$$\left. \frac{\partial T}{\partial x} \right|_{OS} = 0 \quad (3.2)$$

2. The temperatures and heat fluxes on all interfaces between the components of different materials are conjugated. For example, along the line DB:

$$T|_{-DB} = T|_{+DB} \quad (3.3)$$

$$\lambda_{-DB} \left. \frac{\partial T}{\partial x} \right|_{-DB} = \lambda_{+DB} \left. \frac{\partial T}{\partial x} \right|_{+DB} \quad (3.4)$$

3. The Dirichlet constant temperature condition is applied along lines AB, EF, and CD to simulate the heating of the cold, heater, and hot plates, respectively. For example, in the case of the 10°C difference between the hot and the cold plates, with the heater and hot plates kept at 200°C:

$$T_{AB} = T_c = 190^\circ C \quad (3.5)$$

$$T_{EF} = T_{htr} = 200^\circ C \quad (3.6)$$

$$T_{CD} = T_h = 200^\circ C \quad (3.7)$$

The lines AB and CD pass through the centerlines of the heat transfer fluid channels, which is a very close approximation of the actual system. The line EF passes through the middle of the heater plate, representing the electrical heating coil (refer to Chapter 2 for construction of GHP apparatus).

4. The natural convection boundary condition was assumed along the air/insulation interface (SH-HJ-JO), and was expressed by a Newton's law of cooling:

$$q_{cond} = q_{conv} \quad (3.8)$$

$$\lambda_{insulation} \frac{\partial T_{surface}}{\partial n} = h \cdot (T_{surface} - T_\infty) \quad (3.9)$$

The ambient air temperature in the lab, T_∞ , was assumed to be 20°C with a convective heat transfer coefficient, h , of 4 W/m²K.

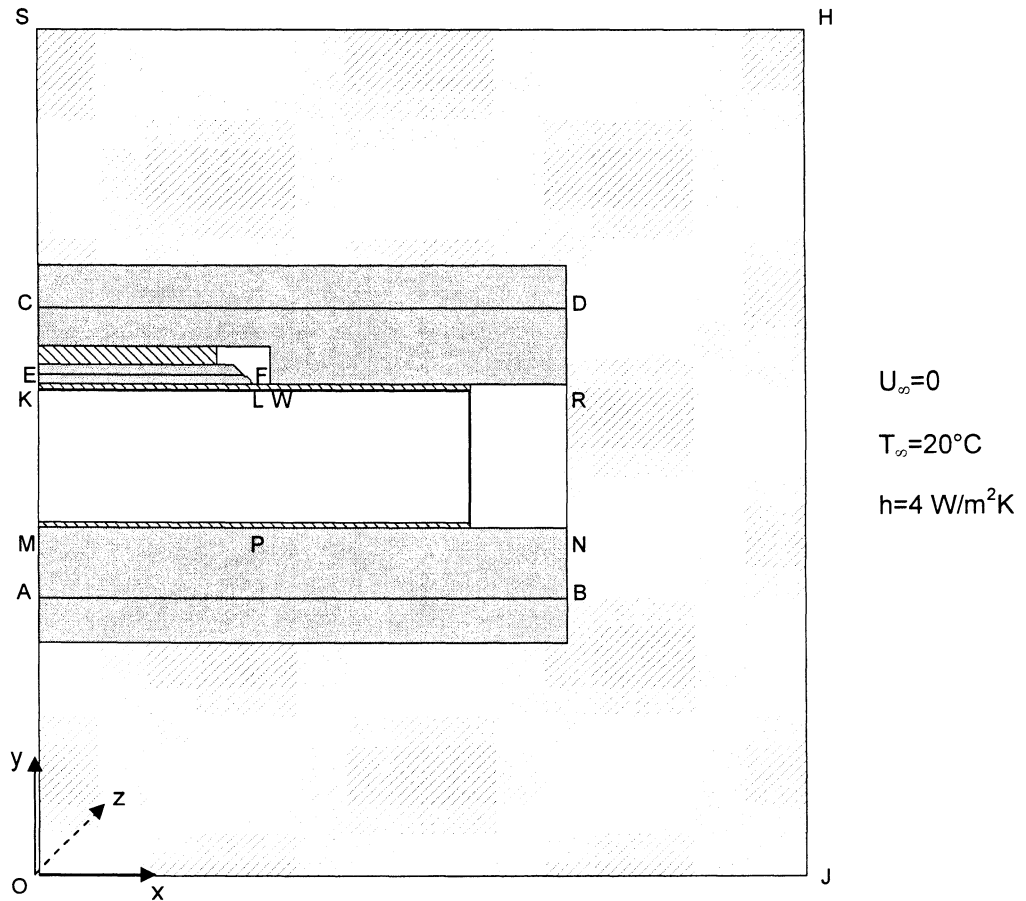


Figure 3.4: Geometry and boundaries of the computational domain.

3.4 Grid Sensitivity Study

To ensure that numerical solutions were independent of the grid density, a detailed grid sensitivity study was conducted. The problem was initially solved on the basis of a coarse grid comprising 982 nodes (coarse grid density). Then, the number of nodes within the computational domain was roughly tripled 2882 (medium grid density), and then tripled again up to 9237 nodes (high grid density). Although there were no numerical instabilities present regarding all three mesh densities (since the governing conduction equation (Equation (3.1)) is

relatively easy to solve numerically), clearly there are not enough nodes in the coarse grid to closely represent the temperature field occurring in the regions of high temperature gradients, complex geometry, as well as on the interfaces between different materials. One of such regions is around the separating air gap between the heater and hot plates (refer to Figure 3.1); it has been chosen to demonstrate the discrepancy between the simulation results with respect to the change in grid density (Figures 3.5, 3.6, and 3.7). One may notice a significant variation between the temperature fields for coarse and medium grid densities. However, the solution did not change significantly with regard to refining the medium grid density from 2882 to 9237 nodes. Meanwhile, the time required to solve the problem involving a high grid density domain increased considerably. Therefore, the medium grid density (Figure 3.3) was used for all simulations.

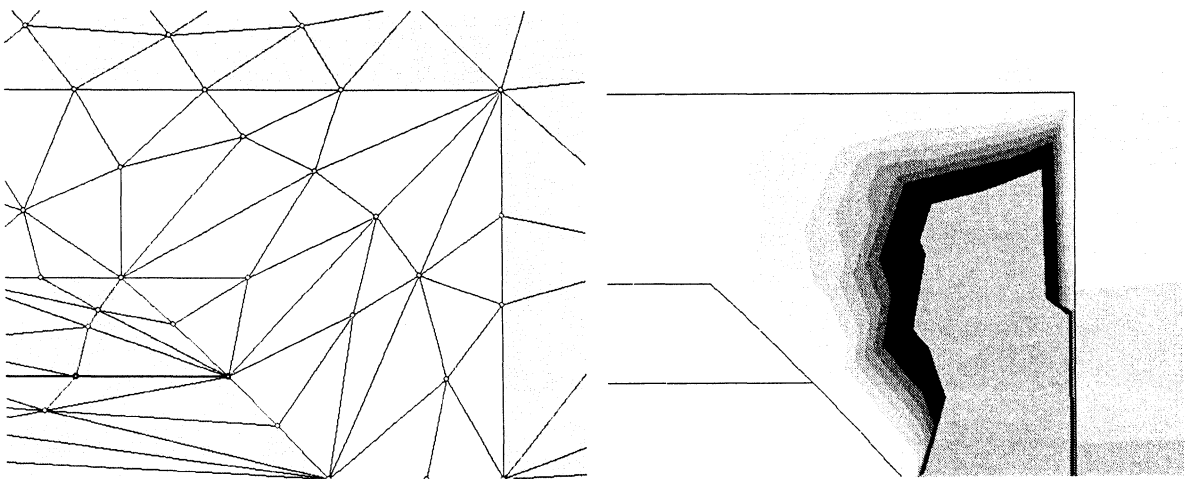


Figure 3.5: Temperature field solution within the air gap region (right) with regard to coarse grid density (left).

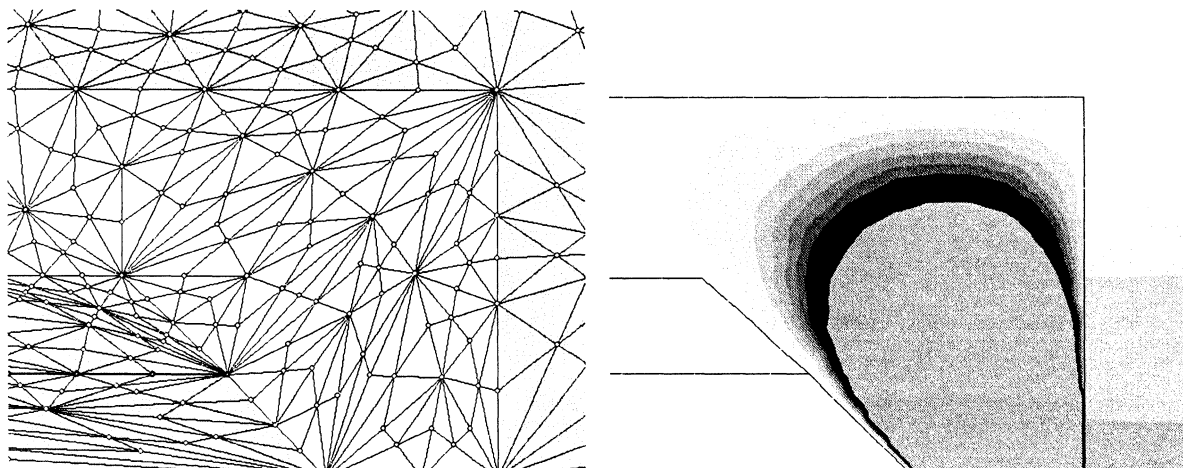


Figure 3.6: Temperature field solution within the air gap region (right) with regard to medium grid density (left).

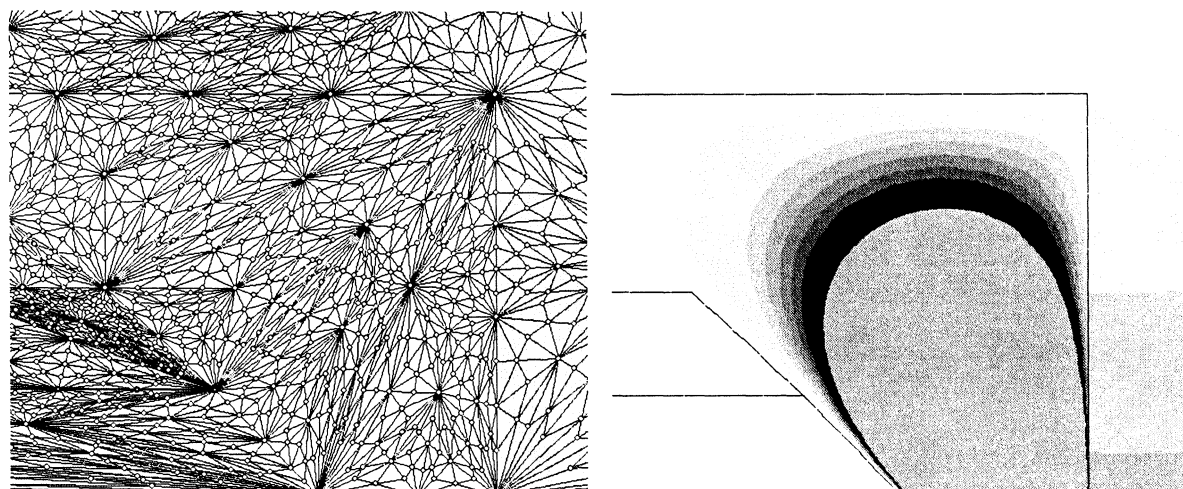


Figure 3.7: Temperature field solution within the air gap region (right) with regard to high grid density (left).

3.5 Analysis of Numerical Results

The results of the simulation indicate that the temperature distribution across the specimen within the region of heater plate (KLPM in Figure 3.4) remains uniform with respect to all three temperature differences of 10, 5, and 2°C between the hot and the cold plates (Figures 3.8, Figure 3.9, and Figure 3.10, respectively).

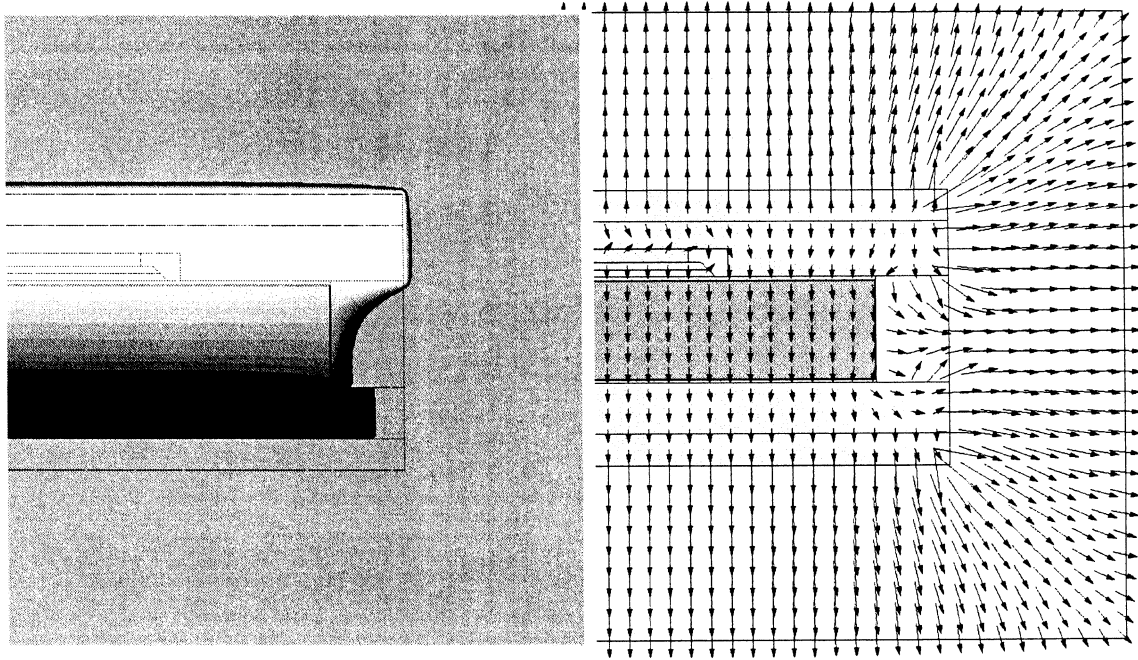


Figure 3.8: Left: Temperature distribution within the computational domain for $\Delta T=10^\circ\text{C}$ between the hot and cold plates (highest isotherm at $T_h=T_{\text{htr}}=200^\circ\text{C}$, lowest isotherm at $T_c=190^\circ\text{C}$). Right: Temperature gradients.

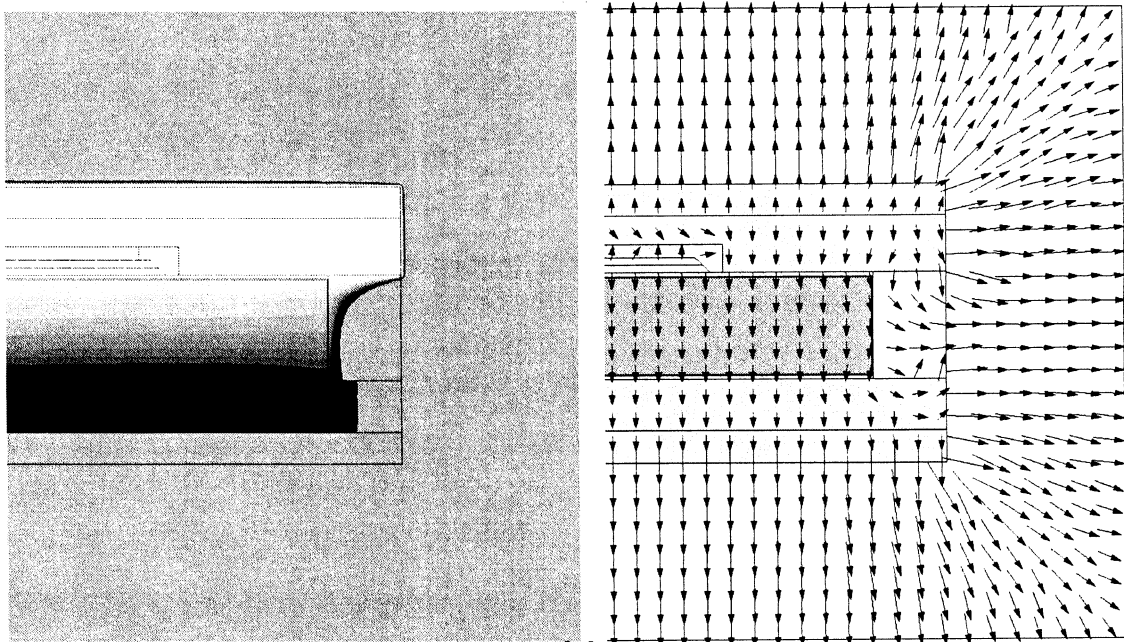


Figure 3.9: Temperature distribution within the computational domain for $\Delta T=5^\circ\text{C}$ between the hot and cold plates (highest isotherm at $T_h=T_{\text{htr}}=200^\circ\text{C}$, lowest isotherm at $T_c=195^\circ\text{C}$). Right: Temperature gradients.

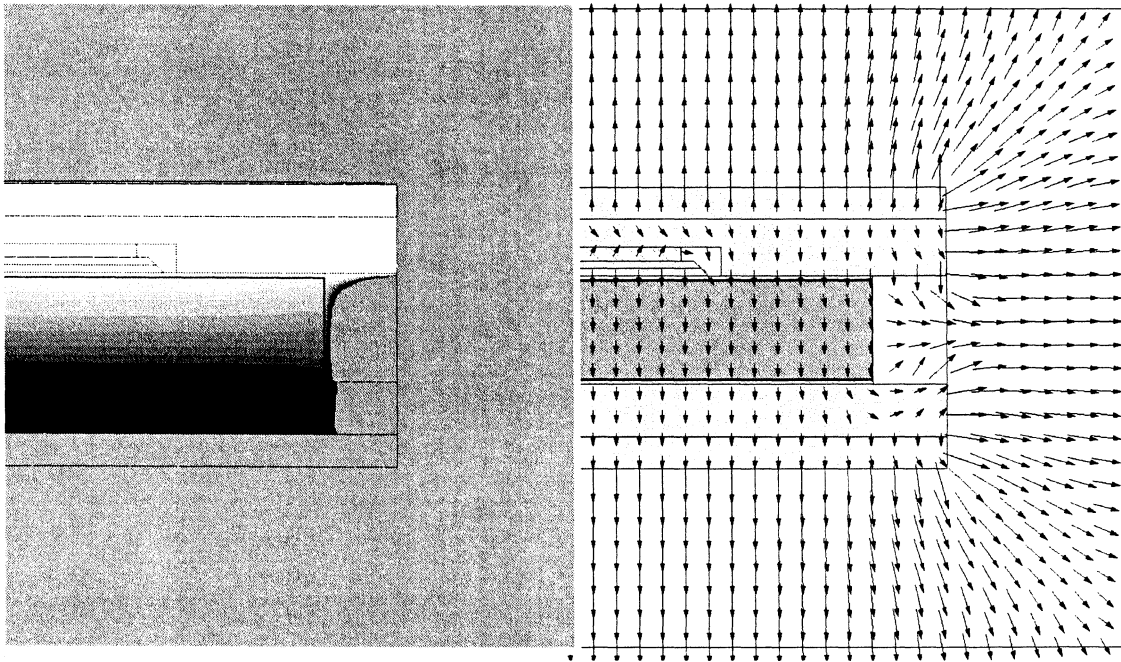


Figure 3.10: Temperature distribution within the computational domain for $\Delta T=2^{\circ}\text{C}$ between the hot and cold plates (highest isotherm at $T_h=T_{\text{htr}}=200^{\circ}\text{C}$, and lowest isotherm at $T_c=198^{\circ}\text{C}$). Right: Temperature gradients.

It should be mentioned that as the temperature difference between the plates decreases, the temperature gradient through the specimen also decreases. However it still remains primarily uniform and downward-unidirectional within the region of heater plate, as shown in the figures above.

We now examine the temperature distribution within the plates themselves. Based on the simulation results shown in Figures 3.11, 3.12 and 3.13, the temperature variations for the 10, 5, and 2°C differences between the hot and cold plates do not exceed 0.025, 0.015, and 0.01°C , respectively. Moreover, the surface temperature distribution within the region of heater plate (KLPM) remains practically uniform for all three temperature differences between the hot and cold plates.

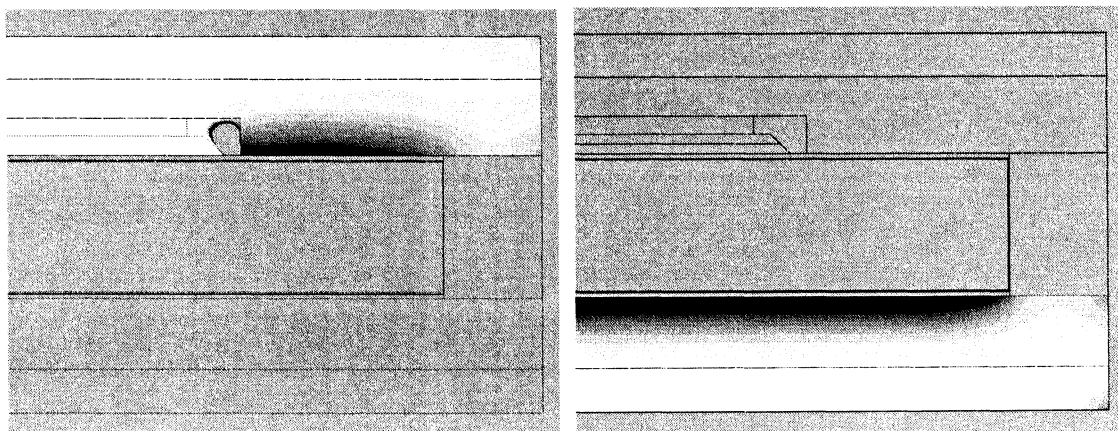


Figure 3.11: Temperature variation of approximately 0.025°C within the hot and heater plates (on the left), and cold plate (on the right) at $\Delta T=10^{\circ}\text{C}$.

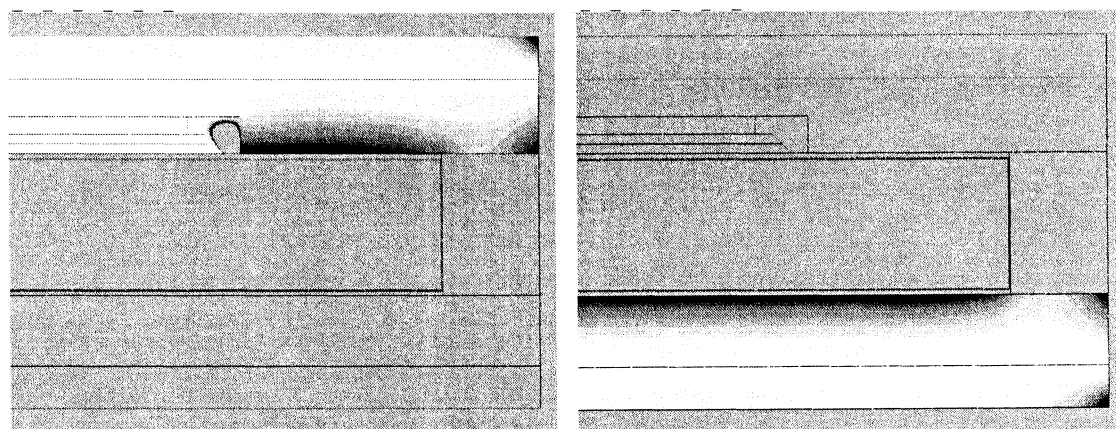


Figure 3.12: Temperature variation of approximately 0.015°C within the hot and heater plates (on the left), and cold plate (on the right) at $\Delta T=5^{\circ}\text{C}$.

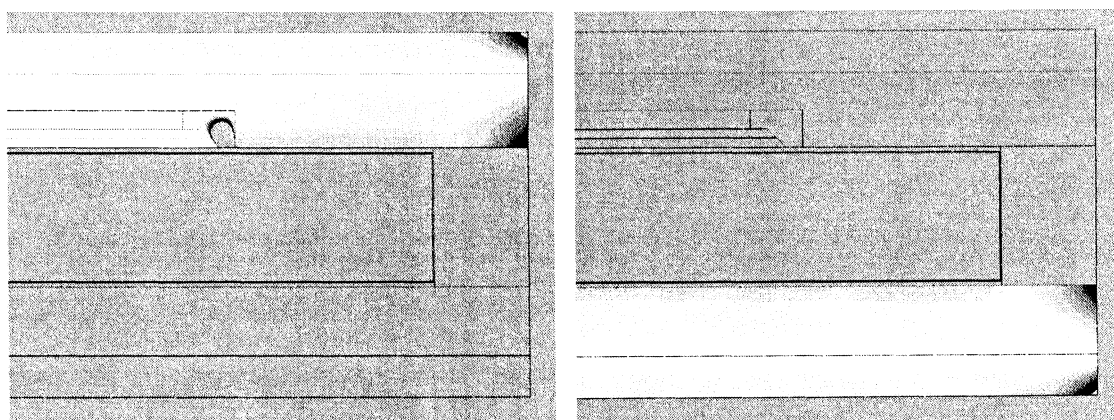


Figure 3.13: Temperature variation of approximately 0.01°C within the hot and heater plates (on the left), and cold plate (on the right) at $\Delta T=2^{\circ}\text{C}$.

This analysis confirms the following for the GHP assembly and particular experimental setup under the extreme case of $T_h = 200^\circ\text{C}$:

1. The heat flow is uniform and unidirectional across the soil specimen at the heater plate region for all three considered ΔT 's, which is a required condition for accurate measurement of thermal conductivity.
2. The isothermality of hot, cold and heater plates are indeed achieved which is a prior condition for achieving uniform and unidirectional heat flow across a soil specimen.
3. The temperature gradient appears to be distorted only in the close vicinity of the edge of the soil specimen container. This indicates that the size of the container is adequate for achieving uniform and unidirectional heat flow across a soil specimen in the heater plate region.

CHAPTER**4****SOIL SAMPLE PREPARATION, PROPERTY MEASUREMENTS,
AND EXPERIMENTAL PROCEDURES**

4.1 Introduction

Soil thermal properties are strongly influenced by the soil volumetric water content as well as by the volume fraction of solid to air. Since air is a poor thermal conductor, it reduces the effectiveness of the partially saturated soil to conduct heat; and while the solid phase has the highest conductivity, it is the variability of moisture within the sample that heavily influences the thermal conductivity. Hence, a successful experimental measurement of soil thermal conductivity requires a careful and reliable sample preparation technique. Dry soil properties such as dry bulk density and soil particle density have to be also precisely measured since without them the thermal data is meaningless. Then water is added to achieve the desired moisture content according to the procedure described below.

4.2 Preparation of Soil Samples

The specimen preparation procedure is based on that first introduced by Holton *et al.* [35]. The methodology varies with respect to the moisture content, and is summarized below for the cases of dry, barely-to-moderately moist, and highly-to-fully saturated moist samples.

4.2.1 Preparation of Dry Soil Samples

Preparation of dry soil samples involves the following procedure:

- 1 The soil sample is dried in an oven for 24 hours at 105°C temperature.
- 2 An arbitrary sample is chosen and its mass and volume are established.
- 3 The soil sample is then poured into an experimental container of 149.42 mm diameter and 20.83 mm depth, made from electroplated 0.20 mm thick mild steel, and covered by an overlapping sliding lid. The soil is poured in layers and each layer is well compacted with a 1 kg weight dropped over a height of about ~10 cm for 5 times to eliminate any air gaps.
- 4 The dry-bulk density, ρ_{db} , of soil sample is determined by:

$$\rho_{db} = \frac{M_{ds}}{V_c} \quad (4.1)$$

where M_{ds} is the mass of the oven dry soil which is hard-packed into a sample container of volume V_c . Bulk density of the soil is an important parameter since it might change for a given soil. It varies with structural condition of the soil and particularly related to packing. Next, the porosity (void fraction) of the soil samples is calculated by:

$$\phi = 1 - \frac{\rho_{db}}{\rho_s} \quad (4.2)$$

where ρ_s is the density of soil solid particles. The solid density is measured by submerging a known mass of soil in water and recording a volume change of the liquid.

- 5 The container is sealed with a *Permatex Aviation Form-A-Gasket #3 sealant*, which is non-hardening, high temperature resistant sealant for pressures up to 5000 psi. The container is then left for 12 hours for the sealant to seal most effectively.
- 6 The weight and the thickness of the filled container are measured and it is then ready for the experiment.

4.2.2 Preparation of Barely-to-Moderately Moist Soil Samples

The following procedure is employed for preparation of soil samples with very low moisture contents (barely moist), when the volumetric water content, θ , is below the permanent wilting point, θ_{PWP} . The volumetric water content (also sometimes called the volume wetness or volume fraction of soil water) represents the fraction of the total volume of soil that is occupied by the water

contained in the soil. The permanent wilting point is defined by the amount of water remaining in the soil in the smallest of micro-pores and around individual soil particles. θ_{PWP} is also defined in the Glossary of Soil Science Society of America Journal as the minimum soil moisture at which a plant wilts and can no longer recover its turgidity when placed in a saturated atmosphere for 12 hours. The same procedure is also applicable to moderately moist soil samples, i.e. when $\theta_{PWP} < \theta < \theta_{FC}$, where θ_{FC} is the soil's field capacity (the maximum moisture content the particular soil can hold in field condition), and the soil gets sticky.

Preparation of barely-to-moderately moist soil samples involves the following procedure:

- 1 The oven dry soil (of mass M_{ds}) is put into previously weighed heavy-duty zip-lock bag. To obtain a specific volumetric moisture content (VMC), θ , the following equation is used to determine the required volume V_w or mass M_w of water to be added to the dry soil:

$$V_w = V_c \theta \quad (4.3)$$

$$M_w = V_c \theta \rho_w \quad (4.4)$$

The bag is then weighed and labeled with θ and M_w values.

- 2 The sample is hand mixed inside the zip-lock bag to achieve a fairly uniform moisture distribution.
- 3 The sealed zip-lock bag is then placed into a microwave oven.
- 4 The microwave reheating is done 5 to 10 times and the sample is left for 6 hours in a constant temperature environment, after which the cyclic microwaving is repeated.

- 5 The weight of the bag is measured again. Note that the possible difference before and after microwaving is caused by the loss of moisture; on this basis, θ of the sample is recalculated.
- 6 The soil sample is then poured into the experimental container in thin layers, and each layer is well compacted as described in section 4.2.1 to eliminate air gaps. The container is then sealed with *Permatex Aviation Form-A-Gasket #3* sealant.
- 7 The container is left for 48 hours in a constant temperature environment for the sealant to seal most effectively and also to achieve a uniform moisture distribution.
- 8 The weight and thickness of the filled container are measured and it is then ready for the experiment.
- 9 After the experiment, the filled container is weighed again to check for any moisture losses.
- 10 To determine the dry-bulk density of the moist soil in the container, open container with moist sample is put in the oven at 105°C for 24 hours to dry it up. The mass of the dry soil is then measured and divided by volume of the container.

4.2.3 Preparation of Highly-to-Fully Saturated Moist Soil Samples

The following procedure is used to prepare soil samples with high moisture contents, when θ exceeds the θ_{FC} :

- 1 The oven dry soil (of mass M_{ds}) is put into a sampler.
- 2 The required amount of water is poured into the sampler and hand mixed by a stirring stick.
- 3 The sample is covered and sealed with a plastic film and weighted.
- 4 The soil sample is then poured into an experimental container in thin layers, and each layer is well compacted as described in section 4.2.1 to eliminate the air gaps. The container is then sealed with a *Permatex Aviation Form-A-Gasket #3 sealant*.
- 5 The container is left for 48 hours in a constant temperature environment for the sealant to cure.
- 6 The weight and the thickness of the filled container are measured and it is ready for the experiment.
- 7 After the experiment the container is weighted again, and then is dried in the oven for 24 hours. The mass of dry mass soil is then determined and divided by volume of the container to get a dry bulk density of moist soil.

4.3 Properties and Composition of Experimental Soils

The two soils used for this experiment were the Ottawa sand and Richmond Hill soil. The Ottawa sand is a natural silica coarse sand with 99% quartz content, a particle density $\rho_s = 2650 \text{ kg/m}^3$, a dry bulk density $\rho_{db} = 1680 \text{ kg/m}^3$ (at well compacted condition), a porosity $\phi = 0.366$, and particles with

diameter variation from 0.59 to 0.84 mm [36]. The Ottawa sand was chosen because it has been studied extensively at low temperatures [36-38] and thus could be used as a reference material for verification of experimental results. Meanwhile, the Richmond Hill soil is grayish-brown in color when dry, and has a fine clay-loam texture determined using the texture chart (Figure 4.3.1). The soil has been extracted from a construction site in the City of Richmond Hill, Ontario, at the northeast corner of Bayview Avenue and Elgin Mills Road from three pits 50~60 cm deep and approximately 50 m apart from each other. The samples were extracted below the top fertile layer (25~30 cm) and hence were not influenced by biological activity nor did they contain organic matter. The Department of Canadian Land Inventory (under the Ontario Ministry of Natural Resources) provided the following textural data for the soil in that area: the sand mass fraction $m_{sa} \approx 0.30$, the silt mass fraction $m_{si} \approx 0.41$, and the clay mass fraction $m_{cl} \approx 0.29$. The average diameters of sand, silt, and clay solid particles are ~0.10 mm, ~0.05 mm, and ~0.001 mm, respectively. The soil also comprises about 13~15 percent rock/gravel fragments, which are ~3 mm in average diameter, however the soil has been sieved through a 2 mm mesh screen to remove them. The average particle density of Richmond Hill soil is around 2650 kg/m³ (as for most North American soils), the dry bulk density is $\rho_{db} = 1137$ kg/m³ (at well compacted condition), and the porosity was calculated to be $\phi = 0.571$, which is typical for its textural class (clayey soils have a greater porosity and lower bulk density than sandy soils).

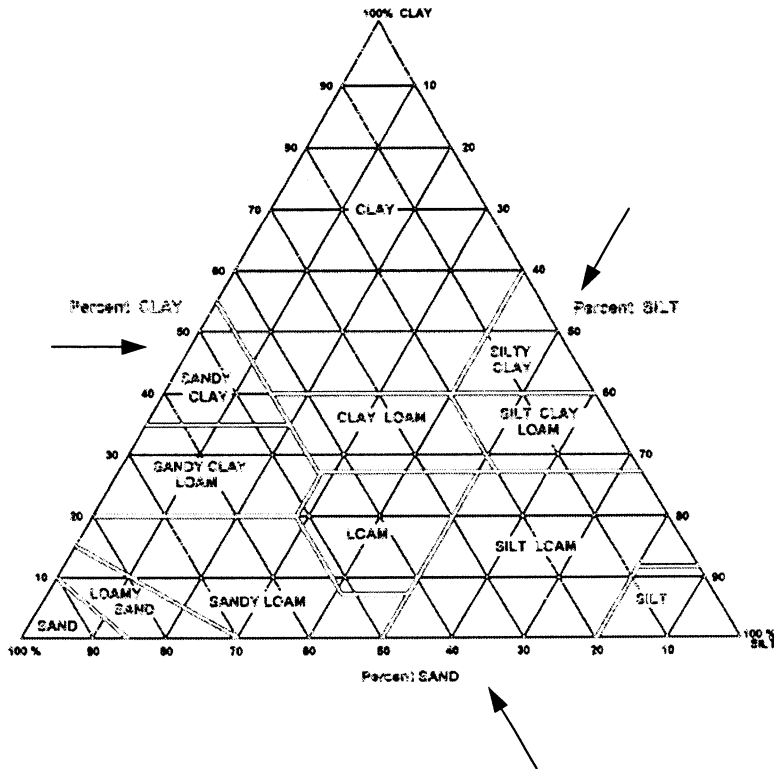


Figure 4.1: Soil texture chart [39]

On the basis of physical properties it is then possible to estimate the θ_{PWP} and θ_{FC} values, which are very important for planning out the experiment. In particular, a useful rule of thumb is to estimate θ_{FC} as $\phi/2$, and θ_{PWP} as $\theta_{FC}/2$. Banin and Amiel [40] and Dahiya et al. [41] have demonstrated that the assumed ratios of

$$\frac{\theta_{FC}}{\phi} = \frac{1}{2} \quad (4.5)$$

and

$$\frac{\theta_{PWP}}{\phi} = \frac{1}{4} \quad (4.6)$$

are good approximations, based on measured correlations on many soils. Table 4.1 tabulates the volumetric moisture contents at permanent wilting point, field capacity and full saturation for Ottawa sand and Richmond Hill clay-loam.

Table 4.1: Permanent wilting point, field capacity and full saturation points of Ottawa sand and Richmond Hill clay-loam.

Volumetric moisture content (m^3/m^3)	Ottawa sand	Richmond Hill clay-loam
θ_{PWP}	0.092	0.143
θ_{FC}	0.183	0.290
θ_{FS}	0.366	0.571

4.4 Experimental Planning and Procedure

In order to capture the complete trend of thermal conductivity variation with moisture content, the following eleven or twelve experimental points of volumetric moisture content are considered: one point at dry condition ($\theta = 0$), two points within the barely moist range ($0 < \theta < \theta_{PWP}$), five points within the moderately moist range ($\theta_{PWP} < \theta < \theta_{FC}$), two or three points within the highly moist range ($\theta_{FC} < \theta < \theta_{FS}$), and one point at fully saturated condition ($\theta = \phi$). Based on these volumetric moisture contents, the soil samples are prepared accordingly.

The starting and final experimental temperatures, the temperature increment, the temperature difference between the cold and hot plates, and the specimen thickness are entered into the *GHP Control v.2.0* computer program. The circulating baths are then automatically powered on. Note that before the experiment all the equipment is started and allowed approximately 30 minutes to

warm up. Meanwhile, the apparatus plates, the heat transfer hoses, and circulating baths are inspected for proper operation. The specimen container is then clamped between the plates (with the silicone rubber pads between the container and plate surfaces), and the frame is locked in the desired angular position. In the cases considered here, the plates are aligned horizontally, with the hot plate on top to prevent any possible natural convective heat transfer in the soil layer. The *GHP Control v.2.0* program will automate the entire measurement procedure from the starting to the final experimental temperatures, and in the end it will shut down the circulating baths.

CHAPTER

5

PRESENTATION AND DISCUSSION OF EXPERIMENTAL RESULTS

5.1 Introduction

Research on the thermal conductivity of two soils, Ottawa sand and Richmond Hill clay-loam, was conducted using the guarded hot plate apparatus at the Ryerson Thermofluids Research Laboratory to study the dependence of soil thermal conductivity on soil moisture content and temperature. The results were obtained for a wide temperature range of 2 to 92°C, at 10°C intervals, with $\Delta T=4^\circ\text{C}$ between the hot and cold plates, and for moisture contents from completely dry to fully saturated conditions. It is important to point out that the ΔT of 4°C is an optimum temperature difference for maximizing the sensitivity of measuring equipment and, yet, minimizing the temperature gradient across the specific thickness of present soil samples through a series of preliminary tests. The resulting temperature gradient for the entire study was about 170K/m, which gave a range of heat flux through the soil samples covering from about 38 to 765 W/m². The overall experimental uncertainty of all thermal conductivity measurements associated with 95% confidence level was determined to be about 3.0% (refer to Section 2.5).

5.2 Experimental Results

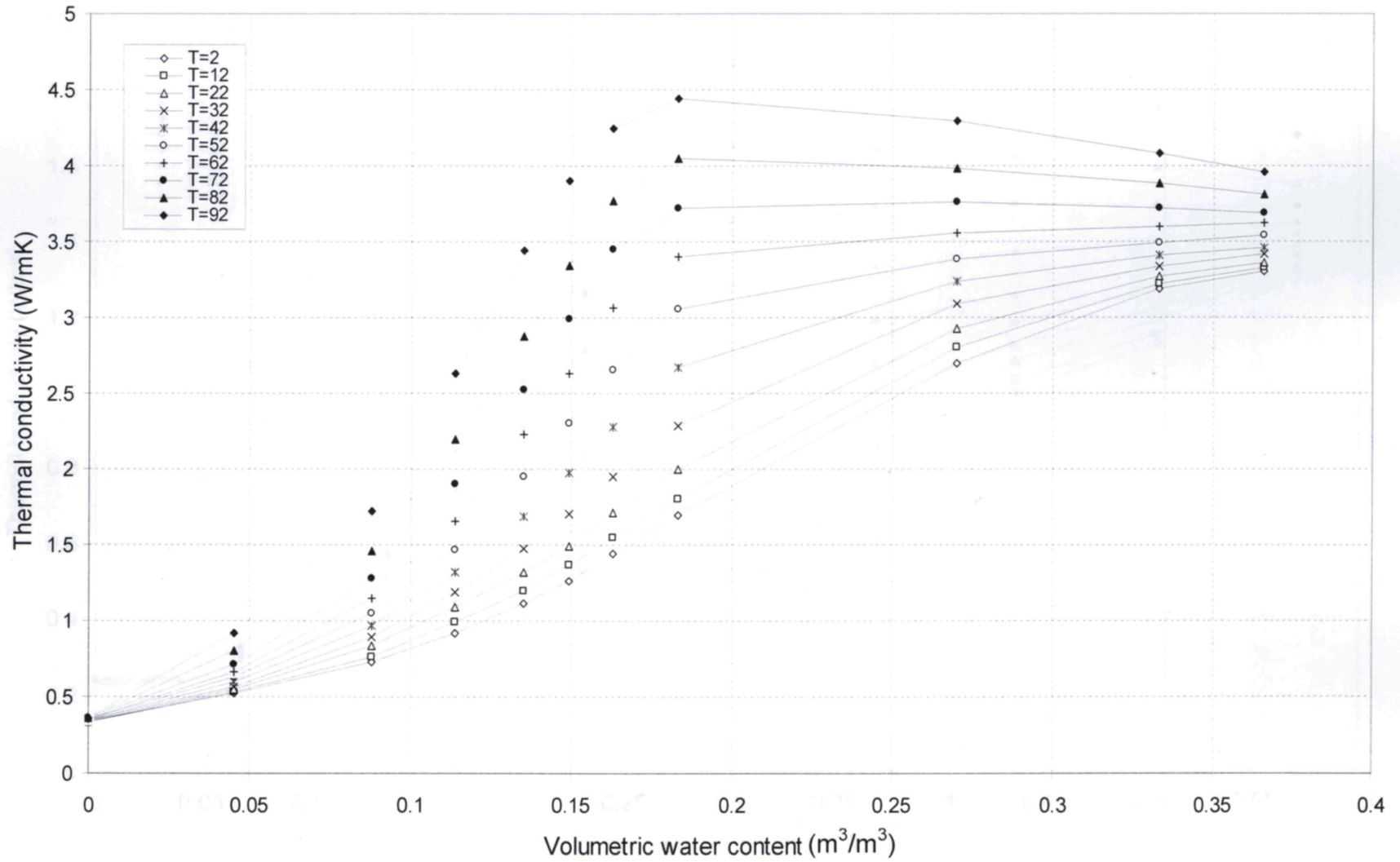
The variation in thermal conductivity of Ottawa sand and Richmond Hill clay-loam with volumetric moisture content for each temperature investigated are plotted in Figures 5.1 and 5.2, respectively (for the tabulated data please refer to Appendix A). The effects of temperature and water content are clearly visible on the graphs, and follow the expected general patterns for quartz sand and clay-loam soils analyzed by Nakshabandi *et al.* in [42]. In particular, in both cases the thermal conductivity increases in three stages with respect to increasing moisture content. At very low moisture contents up to the permanent wilting point, the thermal conductivity of soils increases slowly, since the moisture just coats the soil particles and the voids between the soil particles are not filled with water. At the permanent wilting point the particles are fully coated with water, and as the moisture content further increases, the water fills the gaps between the soil particles. This results in the rapid increase of the heat flow between the particles caused by a rapidly increasing thermal conductivity. The rapid increase is even more prominent for high temperatures, such as those greater than 62°C, resulting in a peak thermal conductivity greater than the one at full saturation, which may be a result of water vapour migration through air passages in the soils [43]. However when the field capacity is exceeded, the voids are mostly filled and a further increase in moisture content does not appreciably increase the heat flow between the particles. Thus the thermal conductivity increases slightly after that point. Moreover, as the temperature exceeds approximately 65~70°C for both soils, the thermal conductivity slowly decreases as the volumetric water

content exceeds 0.2~0.25 and 0.3~0.37 for Ottawa sand and Richmond Hill clay-loam, respectively. This observation may be explained by the formation of small air pockets, which are completely surrounded by soil particles and water; water vapour stays within the air pockets and does not easily migrate, leading to a reduction in heat transfer due to mass transfer.

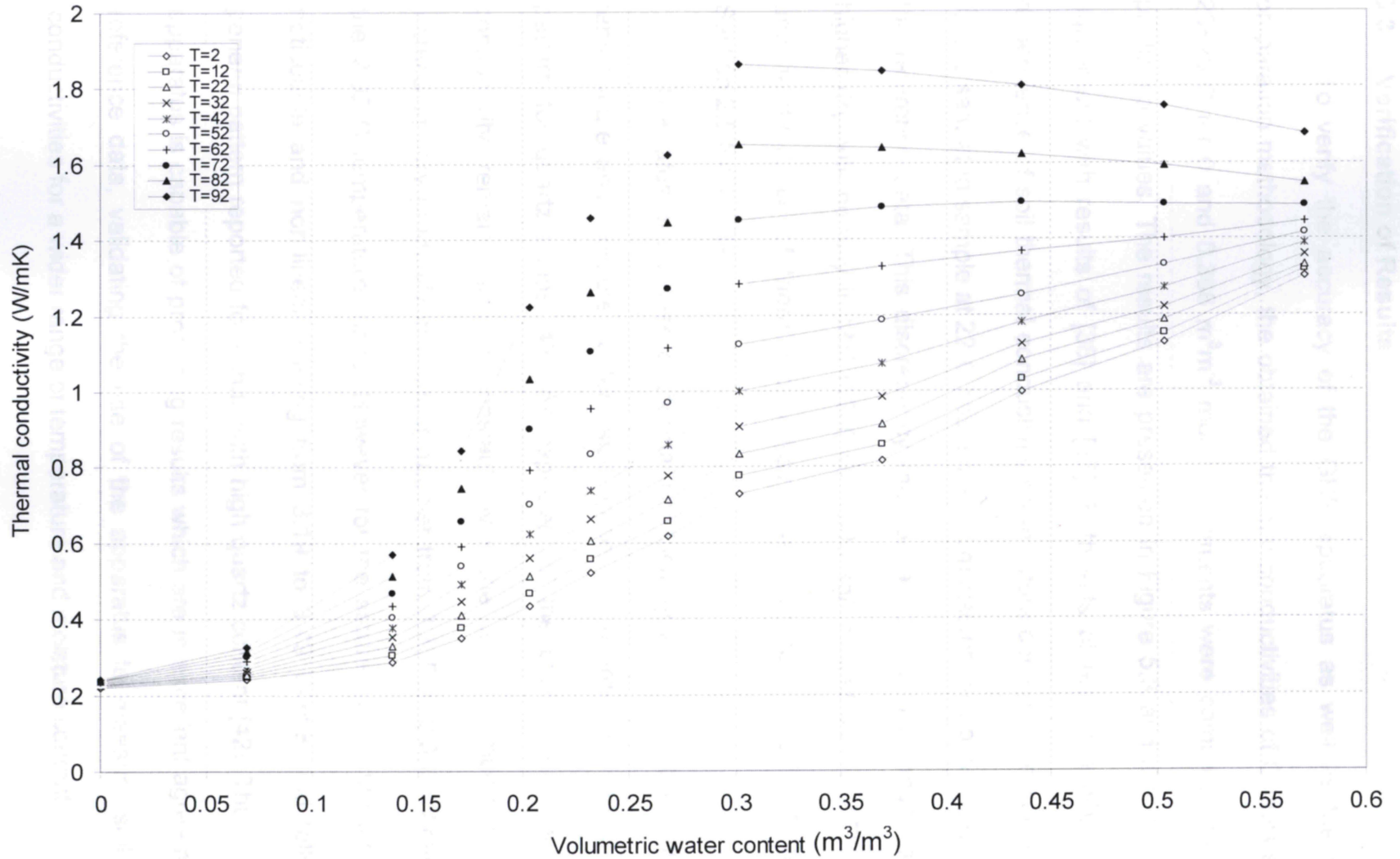
Ottawa sand (a coarse textured soil) has higher thermal conductivities than Richmond Hill clay-loam (a fine textured soil) by an average of 1.5 to 2.6 times, corresponding from dry to fully saturation, for all experimental temperatures. It can also be observed from Figures 5.1 and 5.2 that the thermal conductivities for 2, 12 and 22°C (maybe up to 30°C) are relatively close together; however, for higher temperatures (especially greater than 40°C), the effect of temperature on the thermal conductivity has become more obvious and caused the curves to shift further upward. This may suggest that the heat transfer in the low temperature range (2 ~ 30°C) is dominated by conduction through the moist soils with very limited extent due to vapour migration. When the temperature is high enough (such as greater than 40°C), the heat transfer due to vapour migration becomes noticeable, resulting an apparent or effective thermal conductivity which may be greater than the thermal conductivity due to pure conduction alone in the moist soils.

For moderately-moist soils ($\theta_{PWP} < \theta \leq \theta_{FC}$) at high temperatures, vapour migration (i.e., mass transfer) plays a very significant role in heat transfer, effecting a rapid increase in the thermal conductivity. In fact, for very high temperatures of 82 and 92°C, the peak thermal conductivity near the field

capacity is even greater than the one at full saturation. For example, the peak thermal conductivities of Ottawa sand and Richmond Hill clay-loam at 92°C are 4.45 and 1.86 W/m·K, respectively, which are about 12 and 8 times greater than their respective thermal conductivities at dry condition or about 1.12 and 1.15 times greater than their respective thermal conductivities at full saturation.



Figures 5.1: Variation in thermal conductivity of Ottawa sand with temperature and volumetric moisture content.



Figures 5.2: Variation in thermal conductivity of Richmond Hill soil with temperature and volumetric moisture content.

5.3 Verification of Results

To verify the accuracy of the GHP apparatus as well as the sample preparation methodology, the obtained thermal conductivities of Ottawa sand at 20~25°C for 0 and 0.366 m³m⁻³ moisture contents were compared to several published values. The results are presented in Figure 5.3 and are in excellent agreement with results of [38] and [36]. Both sets of results exhibit a strong dependence of soil thermal conductivity on moisture content. The current result for the saturated sample at 22°C has a maximum discrepancy of 5.2% lower than the reference data. This discrepancy may be attributed to as much as 7.4% higher dry-bulk density in [36] (1680 vs. 1805 kg/m³) and also a 2.7% overall uncertainty ($U_{0.95}$) of thermal conductivity measurement at $\Delta T=4^\circ\text{C}$ (refer to Section 2.5 for details).

The rates of increase of thermal conductivity with respect to increase in temperature and moisture content also agree with a previously noted general pattern for quartz sands [42]. As expected, in the case of dry soil thermal conductivity remains almost constant over the entire temperature range, increasing very gradually in a linear manner from 0.335 to 0.362 W/m·K within the 2-92°C temperature range. However for the saturated soil the increase is noticeable and non-linear, varying from 3.19 to 3.49 W/m·K and following a general pattern reported for sands with high quartz content [42]. Thus, the GHP apparatus is capable of producing results which are in excellent agreement with reference data, validating the use of the apparatus to measure soil thermal conductivities for a wider range of temperature and moisture content.

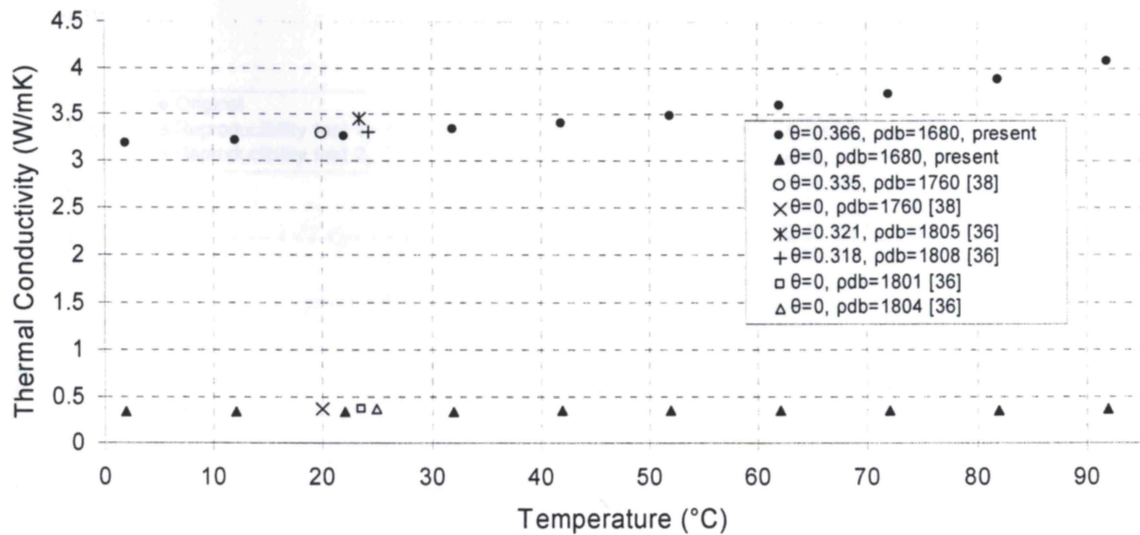


Figure 5.3: Experimental and published thermal conductivity values of Ottawa sand.

5.3 Reproducibility of the Experiment

To illustrate the reproducibility of the results, two experiments were repeated three times for the same Ottawa sand specimen ($0.33 \text{ m}^3 \text{ m}^{-3}$ moisture content). The temperature range and temperature increment were the same for all three experiments. The equipment was turned off for 24 hours before repeating each experiment, and the specimen container was weighed before and after each repetition to ensure that the moisture content remained the same. The results of the reproducibility test are presented in Figure 5.4.

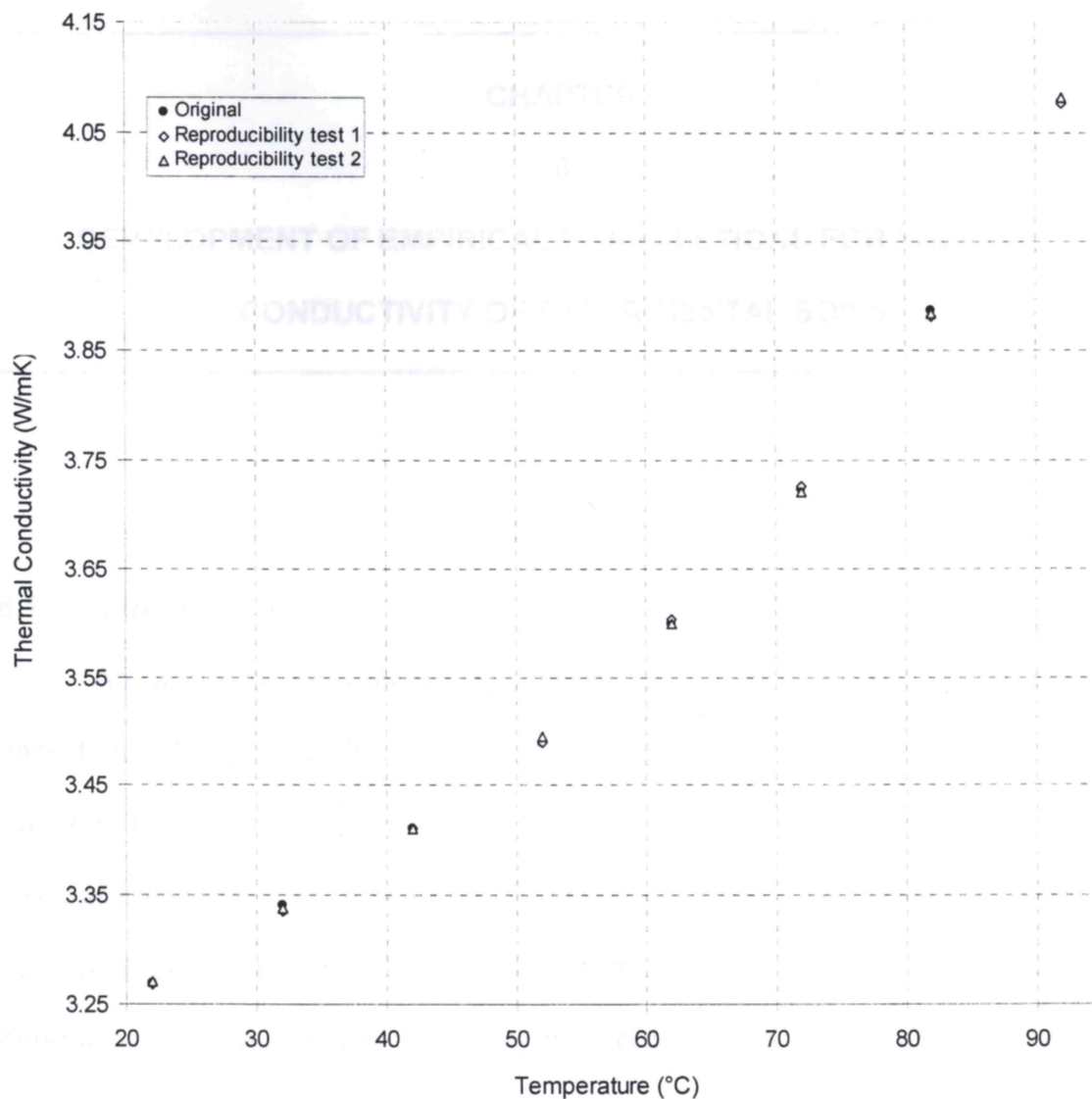


Figure 5.4: Reproducibility test, based on the Ottawa sand specimen with $0.33 \text{ m}^3 \text{m}^{-3}$ moisture content.

Nonetheless, the mean and maximum standard deviations of thermal conductivity regarding three repeated experiments were only 0.0019 and 0.0030 W/mK, respectively, illustrating excellent repeatability of measurements.

5.2 Development of An Empirical Correlation

From the measured data one may notice that the thermal conductivity of Ottawa sand is strongly dependent on temperature and degree of saturation.

CHAPTER

6

DEVELOPMENT OF EMPIRICAL CORRELATIONS FOR THERMAL CONDUCTIVITY OF EXPERIMENTAL SOILS

6.1 Introduction

An accurate knowledge of thermal conductivity of soil is of primary importance for the prediction and numerical simulation of underground heat transfer. The objective of this chapter is to develop empirical correlations for the thermal conductivity of experimental soils which can be easily incorporated into numerical heat transfer algorithms. Correlations are developed for soil thermal conductivity as a function of moisture content and temperature. They are presented for two soil types, namely, sand and clay-loam at unfrozen states, and are based on experimental thermal conductivity values of Ottawa sand and Richmond Hill clay-loam.

6.2 Development of An Empirical Correlation

From the measured data one may notice that the behavior of soil thermal conductivity is strongly dependent on temperature and degree of saturation. An

increase in either leads to an increase in soil thermal conductivity. Thus the prime focus would be to develop a temperature dependent correlation of soil thermal conductivity as a function of moisture content.

It has been briefly noted in the previous chapter that as the moisture content increases from dry to full saturation, the soil thermal conductivity increases in three separate stages. At low saturations (up to the permanent wilting point), the moisture coats the solid particles without filling the air gaps between them. As a result, the thermal conductivity increases relatively slowly and in a near-linear manner. When the saturation reaches θ_{PWP} , the particles are fully coated with moisture, and further moisture addition fills the air gaps between the particles, rapidly increasing the thermal conductivity and consequently increasing the heat flow through the specimen. As the gaps between the particles become nearly filled with moisture, the heat transfer increases very little and the thermal conductivity no longer appreciably increases with further moisture addition. This non-linear behavior can be closely described by an empirical correlation comprised of a combination of hyperbolic functions [22]. In particular, the empirical correlation model used to describe the thermal conductivity as a function of saturation was separated from the following linear combination of hyperbolic functions:

$$\theta = a_1 \left(\sinh(a_2 \lambda^{0.5} + a_3) + \sinh(a_4) \right) \quad (6.1)$$

In particular, to be practical, an empirical correlation model used to describe the thermal conductivity as a function of moisture content was explicitly derived from Equation (6.1):

$$\lambda = \left[\frac{a_3 - \sinh^{-1}\left(\frac{\theta}{a_1} - \sinh(a_4)\right)}{a_2} \right]^2 \quad (6.2)$$

where a_1 , a_2 , a_3 , and a_4 , are coefficients that depend on the type of the soil and temperature. These coefficients are determined using the experimental datasets with the STATISTICA 7.0 software package [44], and are presented in Tables 6.1 and 6.2 for Ottawa sand and Richmond Hill clay-loam, respectively.

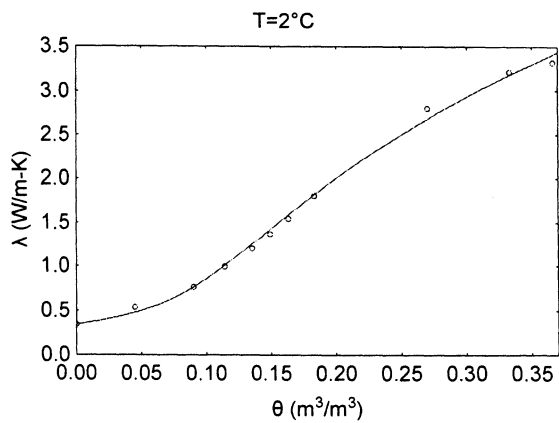
Table 6.1: Temperature dependent correlation coefficients for Ottawa sand.

T (°C)	a_1	a_2	a_3	a_4
2	6.9088×10^{-2}	2.7204	-3.1303	1.5292
12	6.1517×10^{-2}	2.8675	-3.2628	1.5690
22	5.1600×10^{-2}	3.0890	-3.4806	1.6475
32	3.4797×10^{-2}	3.6369	-4.1198	1.9477
42	1.8808×10^{-2}	4.5312	-5.1990	2.4719
52	6.3520×10^{-3}	6.1266	-7.1929	3.4964
62	1.7972×10^{-5}	14.9781	-18.3135	9.3994
72	6.8134×10^{-3}	5.5146	-6.6333	3.2846
82	3.1298×10^{-2}	2.9348	-3.3401	1.5818
92	2.1404×10^{-2}	0.7519	1.9523	-2.3894

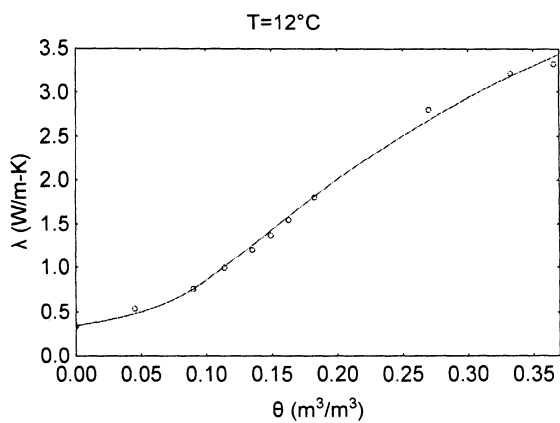
Table 6.2: Temperature dependent correlation coefficients for Richmond Hill clay-loam.

T (°C)	a_1	a_2	a_3	a_4
2	1.2793×10^{-1}	4.4986	-3.5415	1.5397
12	1.2655×10^{-1}	4.5036	-3.5051	1.4793
22	1.1038×10^{-1}	4.8341	-3.7134	1.5096
32	9.3772×10^{-2}	5.1898	-3.9585	1.5691
42	6.8258×10^{-2}	5.9510	-4.5686	1.7892
52	3.5083×10^{-2}	7.7200	-6.0679	2.3803
62	6.7038×10^{-3}	12.2152	-9.9531	3.9913
72	5.3672×10^{-3}	12.0665	-10.0896	4.1645
82	6.4025×10^{-2}	4.6545	-3.8100	1.6128
92	1.4620×10^{-1}	0.9467	0.9407	-1.3311

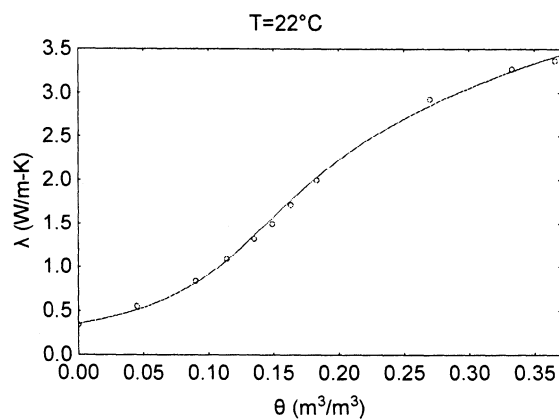
Figures 6.1 and 6.2 present the measured soil thermal conductivity versus volumetric moisture content (VMC) within the entire experimental temperature range (2 to 92°C) for Ottawa sand and Richmond Hill clay-loam, respectively. The empirical correlation (Equation 6.2) is also plotted to visually illustrate the goodness of the fits. Meanwhile, the quantitative analysis of fitting error is presented in the following section.



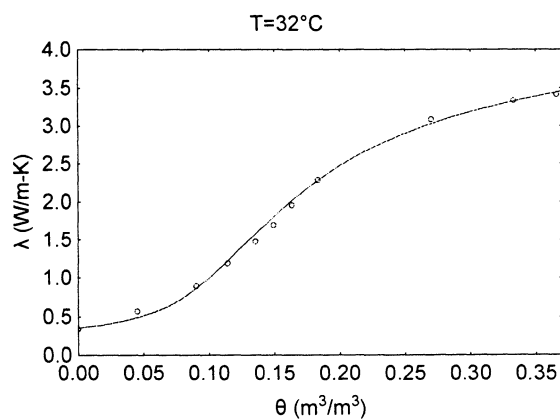
(a)



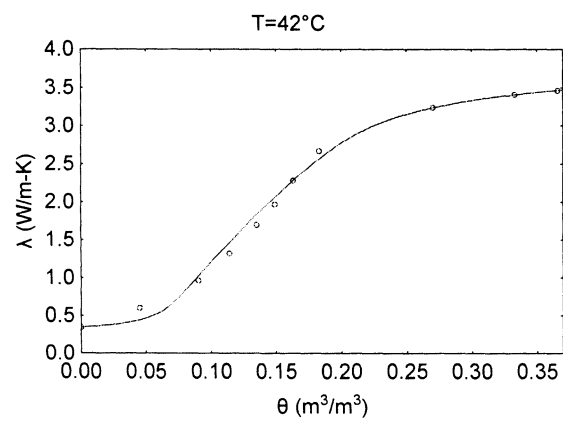
(b)



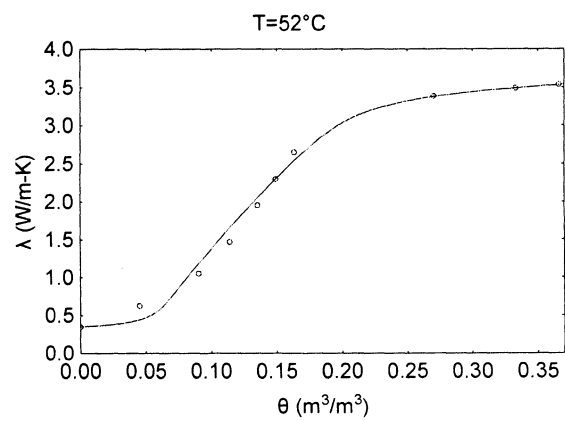
(c)



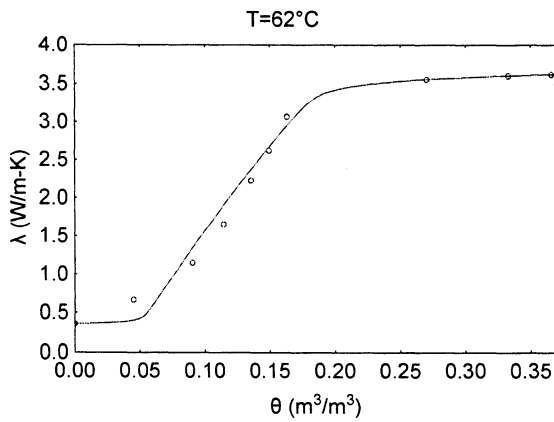
(d)



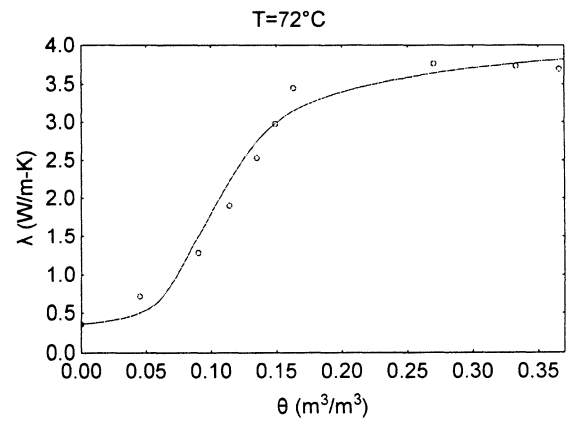
(e)



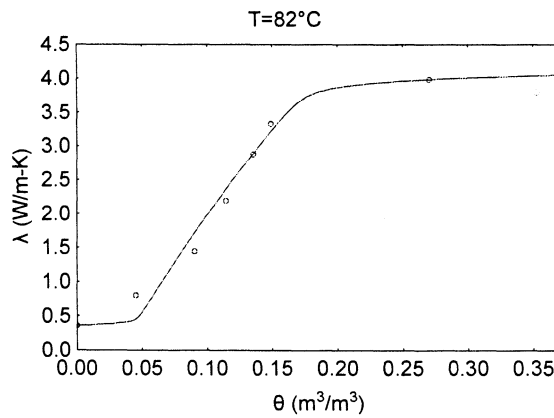
(f)



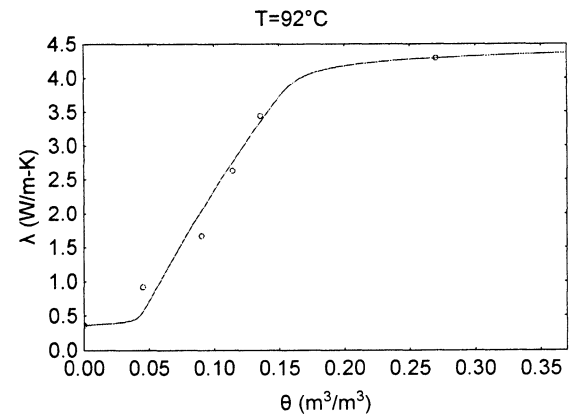
(g)



(h)

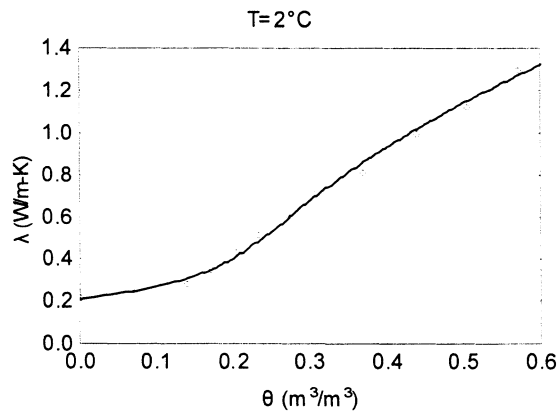


(i)

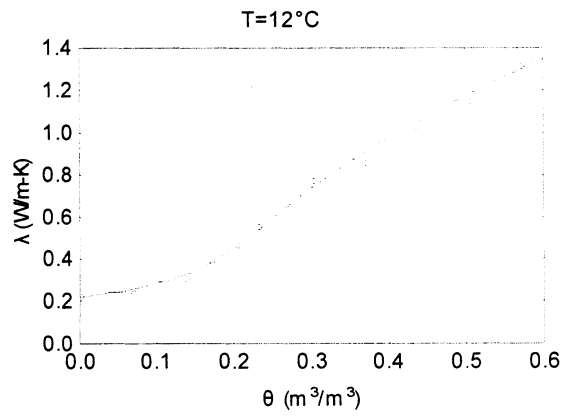


(j)

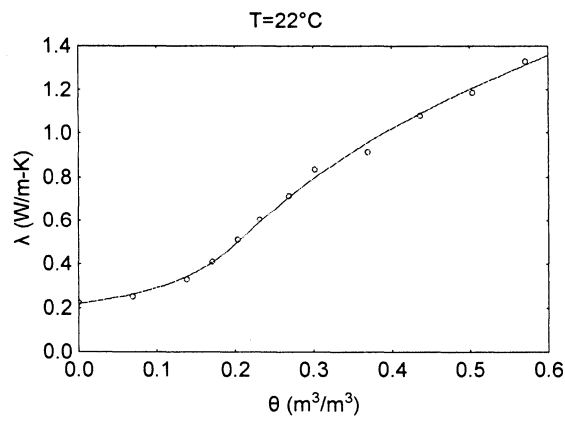
Figure 6.1: Thermal conductivity vs. VMC for Ottawa sand with superimposed empirical correlation for various temperatures. Each experimental temperature considered from 2 to 92°C is shown from (a) to (j).



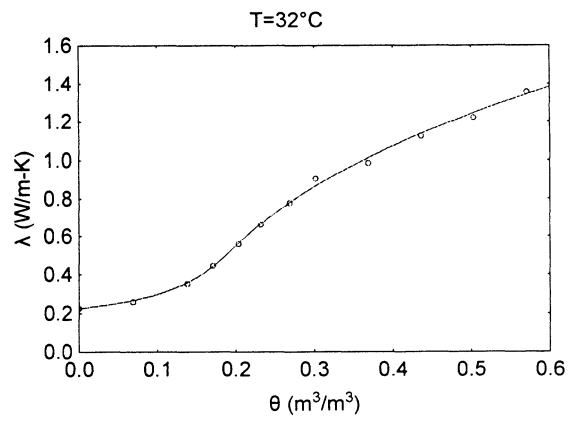
(a)



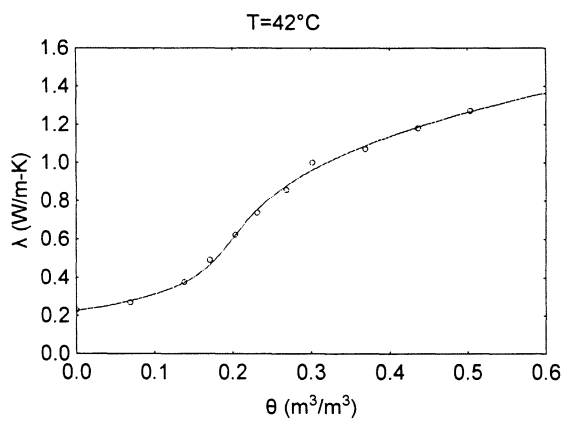
(b)



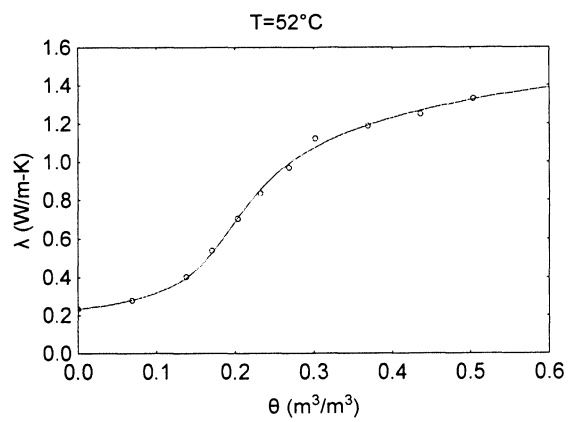
(c)



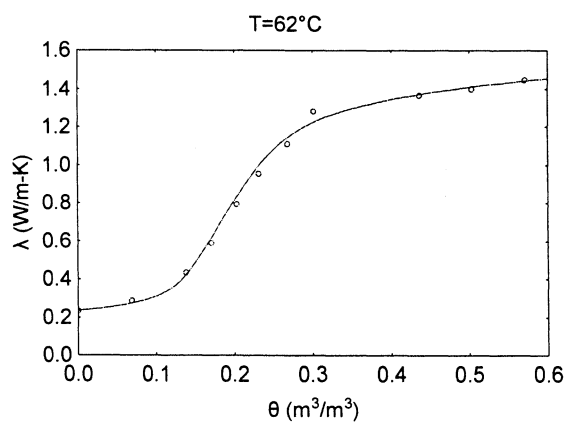
(d)



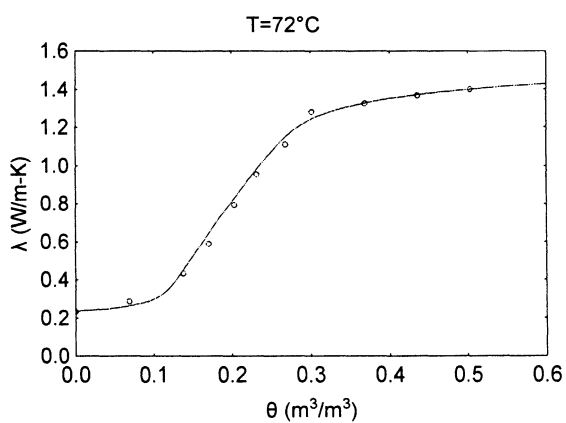
(e)



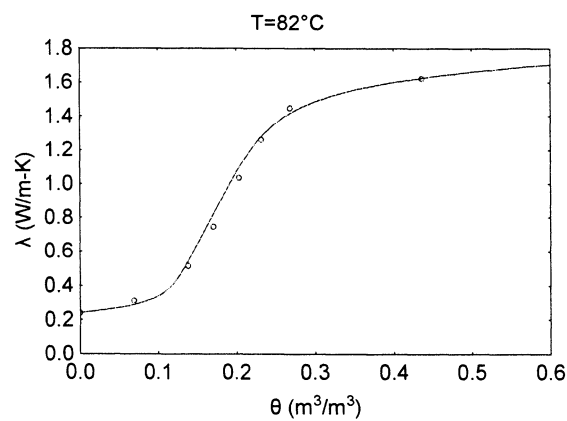
(f)



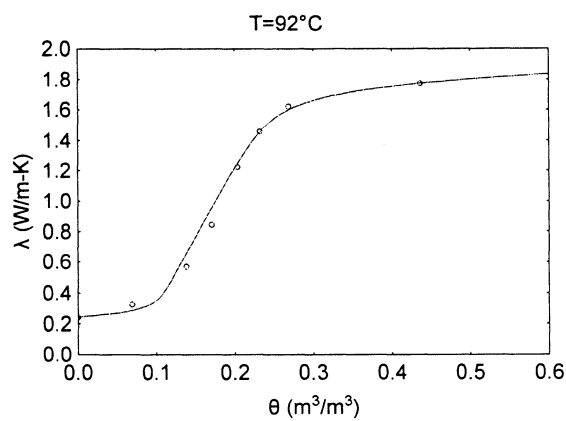
(g)



(h)



(i)



(j)

Figure 6.2: Thermal conductivity vs. VMC for Richmond Hill clay-loam with superimposed empirical correlation for various temperatures. Each experimental temperature considered from 2 to 92°C is shown from (a) to (j).

6.3 Fitting Error of the Empirical Correlation

A visual inspection indicates that the proposed empirical correlation model produces an excellent fit to the measured data for most temperatures over the saturation range considered. To assess the accuracy of the correlation quantitatively, the root-mean-square error (RMSE) and the root-relative-mean-square percentage error (RRMSPE) were calculated (Equations (6.3) and (6.4), respectively). From statistics, RMSE is defined as the square root of the mean squared error (MSE), which is the expected value of the square of the error (the amount by which the estimator differs from the quantity to be estimated). In turn, RRMSPE is the square root of the average sum of relative squared errors expressed as a percentage.

$$RMSE = \sqrt{\frac{1}{n} \sum_{i=1}^n [\lambda_{exp,i} - \lambda_{est,i}]^2} \quad (6.3)$$

$$RRMSPE = \sqrt{\frac{1}{n} \sum_{i=1}^n \left[\frac{\lambda_{exp,i} - \lambda_{est,i}}{\lambda_{exp,i}} \right]^2} \cdot 100\% \quad (6.4)$$

where $\lambda_{est,i}$ is the predicted value by the correlation, and $\lambda_{exp,i}$ is the corresponding experimental value. Generally, the correlation is considered acceptable if the RMSE is small, and RRMSPE is less than the overall experimental uncertainty (which is $U_{0.95}=2.7\%$). RMSE and RRMSPE values listed in Table 6.3 support this validation criterion up to $\sim 65^\circ\text{C}$, with RMSE ≈ 0.0254 and 0.0277 W/m-K and RRMSPE ≈ 2.28 and 1.76% for Ottawa sand and for Richmond Hill clay-loam, respectively, validating the proposed correlation model up to and including 62°C . At the higher temperatures between 72 and

92°C, the model is less accurate with the maximum RMSE ≈ 1.0433 and 0.3784 W/m·K and maximum RRMSPE ≈ 26.6 and 26.3% for Ottawa sand and for Richmond Hill clay-loam, respectively. This is explained by inability of hyperbolic functions to follow the decrease in thermal conductivity beyond the field capacity at higher temperatures.

Another useful criterion for evaluation of goodness of fit is the coefficient of determination, r^2 , because it gives the proportion of the variance (fluctuation) of predictable variable from the actual experimental variable. It is a measure that allows the certainty in making predictions using a correlation model to be determined. By definition, the coefficient of determination is the ratio of the explained variation to the total variation (i.e. the fraction of the total squared error that is explained by the model):

$$r^2 = \frac{\sum_{i=1}^n \left[\lambda_{\text{exp},i} - \frac{1}{n} \sum_{i=1}^n \lambda_{\text{exp},i} \right]^2 - \sum_{i=1}^n [\lambda_{\text{exp},i} - \lambda_{\text{est},i}]^2}{\sum_{i=1}^n \left[\lambda_{\text{exp},i} - \frac{1}{n} \sum_{i=1}^n \lambda_{\text{exp},i} \right]^2} \quad (6.5)$$

The coefficient of determination varies between 0 and 1, and the values approaching 1 are desirable. From Table 6.3, the smallest values of coefficient of determination are 0.965 and 0.980 for Ottawa sand and for Richmond Hill clay-loam, respectively, for up to 62°C. For 72 to 92°C, the coefficients of determination are much lower; again, this indicates the inability of hyperbolic functions to follow the decrease in thermal conductivity beyond the field capacity at these temperatures. Therefore, the correlation (Equation (6.2)) is recommended for use up to 62°C.

Table 6.3: Statistical evaluation of the goodness of fit for the developed model (Equation (6.2)) for Ottawa sand (Table 6.1) and Richmond Hill clay-loam (Table 6.2).

Ottawa sand				Richmond Hill clay-loam			
T (°C)	r ²	RMSE (W/m·K)	RRMSPE (%)	T (°C)	r ²	RMSE (W/m·K)	RRMSPE (%)
2	0.998	0.0130	0.167	2	0.980	0.0162	0.534
12	0.997	0.0164	0.134	12	0.989	0.0143	0.404
22	0.997	0.0171	0.154	22	0.992	0.0192	0.345
32	0.995	0.0262	0.267	32	0.993	0.0148	0.310
42	0.996	0.0065	1.746	42	0.994	0.0197	0.243
52	0.993	0.0193	1.967	52	0.994	0.0142	0.812
62	0.965	0.0254	2.275	62	0.985	0.0277	1.759
72	0.612	0.2831	13.5	72	0.672	0.0756	8.4
82	0.406	0.4557	12.6	82	0.497	0.1743	12.6
92	0.117	1.0433	26.6	92	0.275	0.3784	26.3

6.4 An Alternative Correlation Model

An empirical correlation model of soil thermal conductivity by Tarnawski et al. [45] was considered as a more practical alternative. The thermal conductivity is modeled as a function of both temperature and moisture content (Equation (6.6)). Incorporating the temperature into the equation makes it quicker and easier to be used without a table of correlation coefficients regarding each experimental temperature, and thus, without the necessity of interpolating between experimental temperatures.

$$\lambda = \frac{a_1 + a_2T + a_3\theta + a_4\theta^2}{1 + a_5T + a_6\theta + a_7\theta^2} \quad (6.6)$$

The correlation coefficients a_1 to a_7 are obtained for each specific soil and remain constant for all temperatures and moisture contents. In particular, for the Ottawa sand and Richmond Hill clay loam the respective coefficients are determined and listed in Table 6.4.

Table 6.4: Tarnawski correlation coefficients for Ottawa sand and Richmond Hill clay-loam.

Correlation coefficient	Ottawa sand	Richmond Hill clay-loam
a_1	0.3039	0.2079
a_2	-1.3300×10^{-3}	-9.4004×10^{-4}
a_3	-0.6934	-0.7811
a_4	42.9621	6.9407
a_5	-6.1050×10^{-3}	-5.8852×10^{-3}
a_6	-3.8360	-2.7028
a_7	17.6166	7.0293

The goodness of fit of Tarnawski correlation is discussed next. Although the overall coefficients of determination for Ottawa sand and Richmond Hill clay-loam were calculated to be 0.987 and 0.990 (indicating very good fit to the data), respectively, they might be misleading since they were evaluated based on all data covering all temperatures and all moisture contents (on the contrary to the developed model presented in sections 6.2 and 6.3, where r^2 was individually evaluated for each experimental temperature). Thus, the high overall r^2 values in this case do not guarantee the accuracy of correlation for every temperature and moisture content as it can be seen from Figures 6.3 and 6.4 for Ottawa sand and Richmond Hill clay-loam, respectively. For example, the largest fitting error for

Ottawa sand and Richmond Hill clay-loam are 20.6% and 17.1%, respectively, which are much larger than the overall experimental error of 2.7%, revealing the possibility of high fitting discrepancy. Apparently, the Tarnawski correlation systematically under-predicts the thermal conductivity of Ottawa and Richmond Hill soils at low moisture contents below permanent wilting point by an average of 13% and 7%, respectively. At temperatures from 40 to 70°C for moisture contents between PWP and FC, Tarnawski model predicts the thermal conductivity with an average error of 8 and 6% for Ottawa and Richmond Hill soils, respectively. Moreover, the overall RRMSPE values for Ottawa sand and Richmond Hill clay-loam are 7.71% and 5.38%, respectively, and are both higher than the experimental $U_{0.95}$ of 2.7%. On these bases it is concluded that the Tarnawski correlation (Eq. (6.6) and Table 6.5) is suited for quick engineering estimates, when the accurate thermal conductivity estimates are not required.

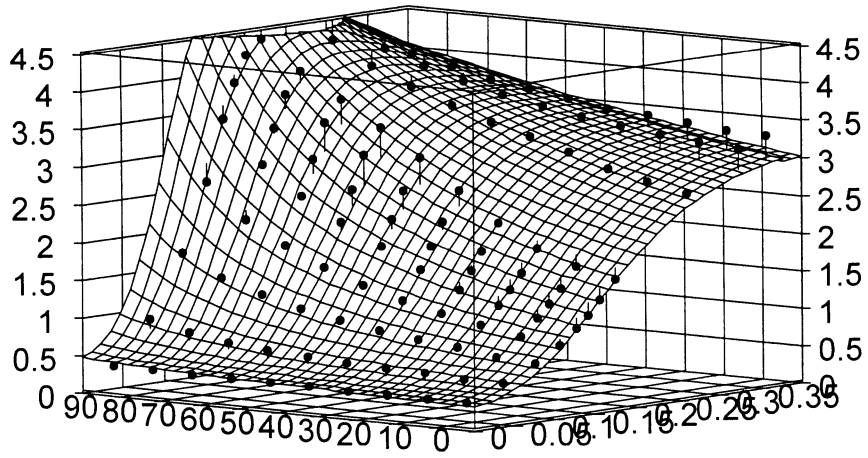


Figure 6.3: Tarnawski empirical correlation for thermal conductivity of Ottawa sand.

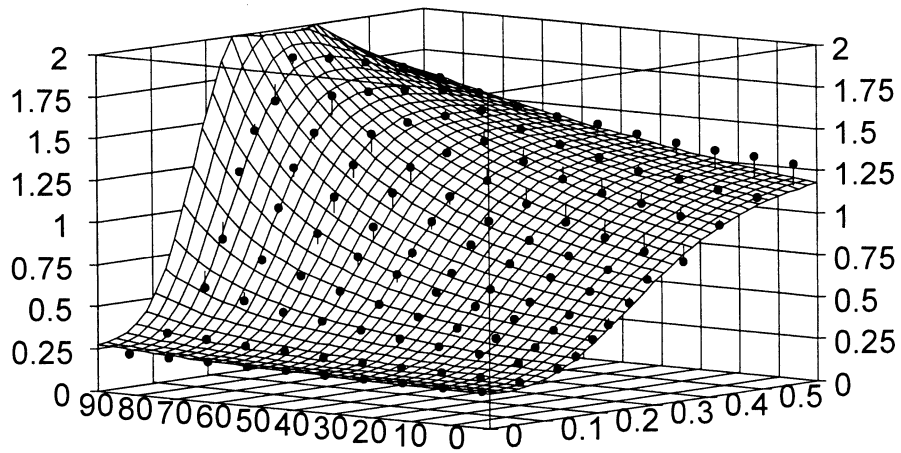


Figure 6.4: Tarnawski empirical correlation for thermal conductivity of Richmond Hill clay-loam.

CHAPTER

7

NUMERICAL SIMULATION OF HEAT LOSS FROM A BASEMENT SURROUNDED BY COARSE AND FINE SOILS OF DIFFERENT MOISTURE CONTENTS

7.1 Introduction

To illustrate the importance of the effective soil thermal conductivity for underground heat transfer problems, a numerical simulation of heat loss from a basement surrounded by Ottawa sand and Richmond Hill clay-loam is performed. The simulation is carried out using the FEHT finite-element software package in 2-D, which is reasonable for such a problem given its symmetry and continuous constant cross-section over a relatively long length before reaching a corner (thus neglecting the corner effect) in the third dimension. The system is assumed to be at steady-state, with a uniform moisture distribution within the soil. A uniform moisture distribution in soil is assumed because the FEHT software can handle thermal conductivity variation as a function of temperature only. The thermal conductivity of the ground, accounting for soil texture, moisture content and temperature, is estimated using the developed empirical correlation (refer to Equation (6.6)). The model in Figure 7.1 presents a 3 m high (DE) and 0.2032 m

thick (CD) basement wall made of concrete which is 2 m below grade (BM); the concrete basement floor is 0.1016 m thick (FN) and 2.5 m long (EF). The soil domain extends 5 m away (AB) and about 3 m deep (AH). The inside basement temperature, T_{inside} , is 20°C. The outside temperature of ambient air, T_{∞} , is 0°C.

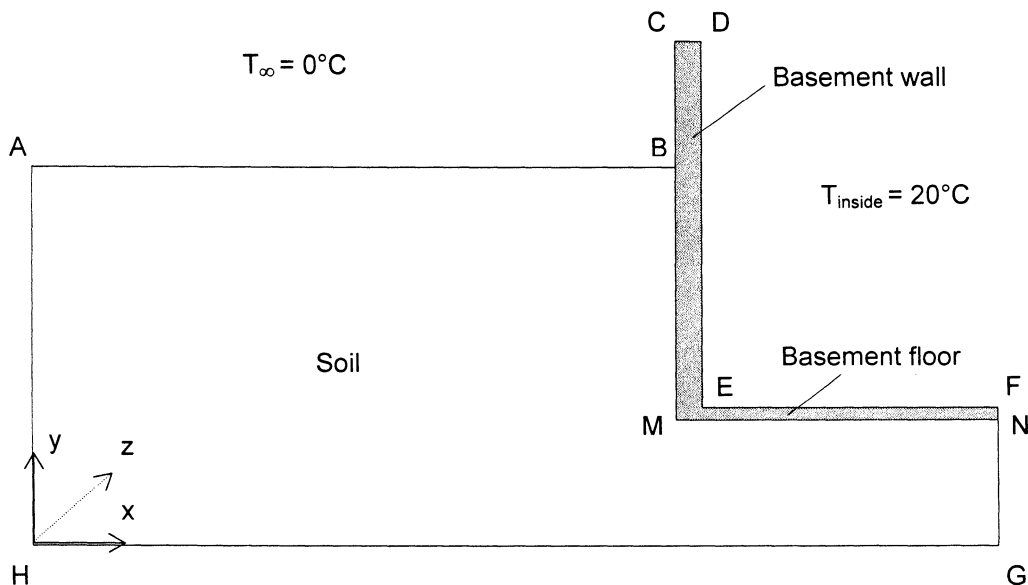


Figure 7.1: Model of basement surrounded by soil.

7.2 Discretization of Domain and Grid Sensitivity Study

The computational domain (Figure 7.1) was discretized into linear triangular elements using the automatic meshing algorithm available in FEHT. The finite-element grid was then modified manually and made denser in the regions where high temperature gradients were expected as well as in the areas of sudden geometrical changes where the boundaries were needed to be described in detail. To ensure that numerical solutions were independent of the grid density, a grid sensitivity study was conducted. The problem, considering dry

Ottawa sand, was initially solved on the basis of a coarse grid comprising 224 nodes and 372 elements (coarse grid density, Figure 7.2). Then, the mesh was made finer to 819 nodes and 1488 elements (medium grid density, Figure 7.3), and then even finer to 3125 nodes and 5952 elements (high grid density, Figure 7.4).

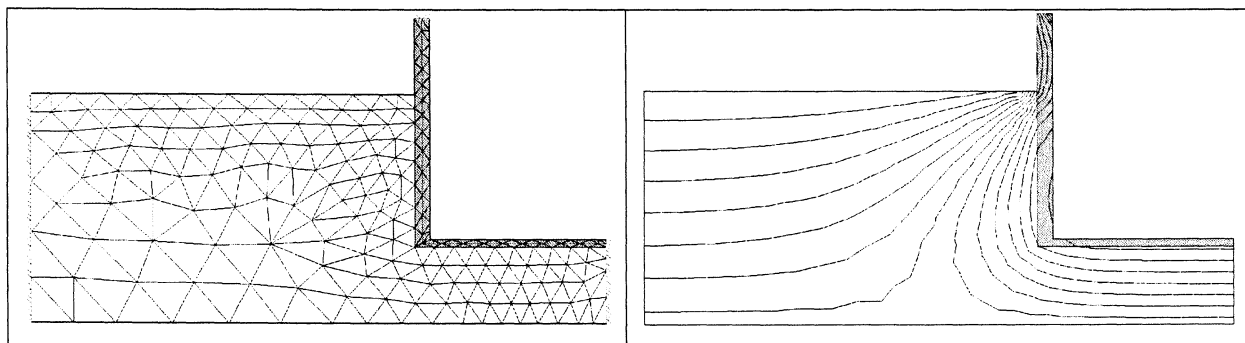


Figure 7.2: Coarse grid density (left), and respective temperature field (right).
15 isothermal lines with $T_{\min}=0.28^{\circ}\text{C}$, $T_{\max}=20^{\circ}\text{C}$

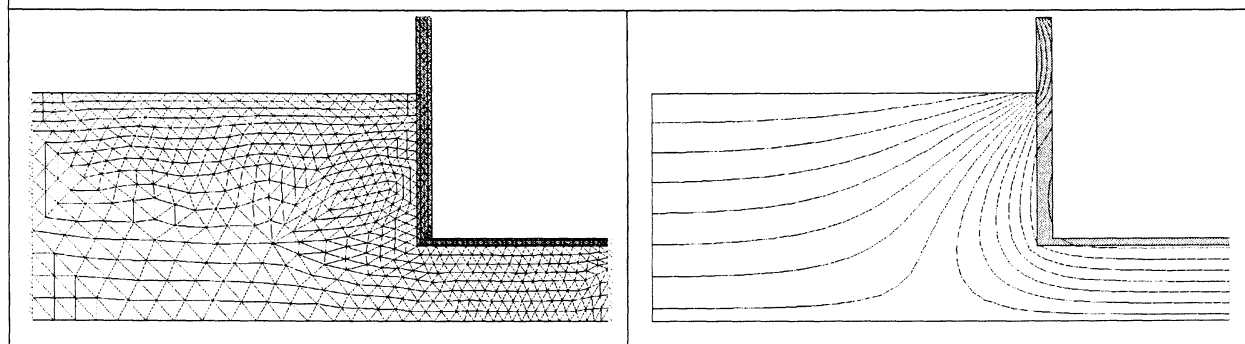


Figure 7.3: Medium grid density (left), and respective temperature field (right).
15 isothermal lines with $T_{\min}=0.29^{\circ}\text{C}$, $T_{\max}=20^{\circ}\text{C}$

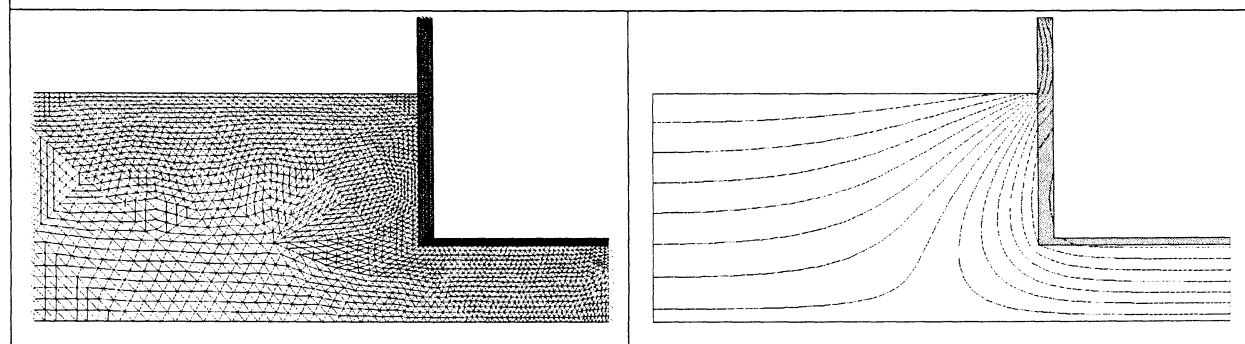


Figure 7.4: High grid density (left), and respective temperature field (right).
15 isothermal lines with $T_{\min}=0.29^{\circ}\text{C}$, $T_{\max}=20^{\circ}\text{C}$

Although there were no numerical instabilities present regarding all three mesh densities, there are not enough nodes in the coarse grid to closely represent the temperature field. The quantitative analysis was based on relative percentage difference (RPD) between the heat flows through the outside underground surfaces of the wall and the floor for three mesh densities. The heat flows were determined to be 21.37, 18.68 and 18.41 W/m for coarse, medium and fine grids, respectively, and the RPDs were computed as follows:

$$RPD = \frac{q_{grid1} - q_{grid2}}{\left(\frac{q_{grid1} + q_{grid2}}{2} \right)} \cdot 100\% \quad (7.1)$$

where q_{grid1} and q_{grid2} are the heat flows (per unit length in z direction) regarding coarse and medium, and then medium and fine grids. The RPD between coarse and medium grids is 15%; meanwhile the RPD between the medium and fine grids is less than 1.4%, illustrating close convergence. Hence both medium and fine grids can be used for the analysis; but since difference in computational time regarding medium and fine grids was not significant, the high grid density was employed for all simulations.

7.3 Mathematical Formulation and Boundary Conditions

The system is governed by the heat conduction equation in two dimensions, assuming steady state conditions, isotropic conductivity, and no heat storage or heat generation within the elements:

$$\frac{\partial}{\partial x} \left(\lambda \frac{\partial T}{\partial x} \right) + \frac{\partial}{\partial y} \left(\lambda \frac{\partial T}{\partial y} \right) = 0 \quad (7.2)$$

where the thermal conductivity λ is assumed to be homogeneous and constant for the concrete wall and floor, and a function of temperature for a given uniform moisture distribution in the soil.

Listed below are the boundary conditions for the computational domain shown in Figure 7.1:

5. The far-field boundary condition is applied to the lines AH and CD, and adiabatic boundary condition is applied to the line FG (as a center line of a basement):

$$\left. \frac{\partial T}{\partial x} \right|_{AH, CD, FG} = 0 \quad (7.3)$$

6. The temperatures and heat fluxes on all interfaces (BM-MN) between different materials are conjugated (Equations (3.3) and (3.4)).
7. The Dirichlet constant temperature condition is applied along line HG to simulate the constant deep ground temperature of 10°C.
8. The natural convection boundary conditions (Equation (3.9)) were assumed along the inside wall surface (DE-EF), outside portion of the wall surface above the ground (BC), and ground surface (AB). The outside ambient and inside air temperatures were set to 0 and 20°C, respectively, with a convective heat transfer coefficient, h , of 4 W/m²K for all convective surfaces.

7.4 Heat Transfer: Effect of Thermal Conductivity Variation with Soil Texture, Moisture Content and Temperature

The heat transfer analysis is based on a comparison of heat flows through the below-grade wall and the floor (BM-MN) for two experimental soils, namely Ottawa sand (coarse texture) and Richmond Hill clay-loam (fine texture), at several moisture contents. In particular, both soils are considered at dry, field capacity (FC), and full saturation (FS) conditions (refer to Table 4.1). The soil thermal conductivity is estimated using the empirical correlations developed in Chapter 6 (Equation (6.6)).

First, the heat transfer is analyzed to investigate the effect of variation in thermal conductivity for the coarse (Ottawa sand) and fine (Richmond Hill clay-loam) soil textures. The numerical temperature distributions for both soils are presented in Figures 7.5 and 7.6, respectively. To make a quantitative comparison regarding the texture variation, the relative percentage difference between the heat flows was calculated as follows:

$$RPD = \frac{q_{coarse} - q_{fine}}{\left(\frac{q_{coarse} + q_{fine}}{2} \right)} \cdot 100\% \quad (7.4)$$

where q_{coarse} and q_{fine} are the heat flows per unit depth in z direction through the underground wall (BM-MN) surrounded by coarse and fine soils (refer to Table 7.1). The highest RPD was calculated to be 62% at field capacity condition, with the heat flows of 33.7 and 64 W/m in the cases of fine and coarse textures, respectively. This relatively large variation indicates the significance of using correct soil texture properties for estimating the effective soil thermal conductivity

and, consequently, for accurate modeling of the ground heat transfer. Based on this finding, in order to have low heat loss from a basement, fine soil can be used as a backfill between the basement walls and the surrounding soil.

Table 7.1: Heat flows through the below-grade wall and the floor with respect to coarse and fine soil textures at several moisture contents.

	Dry	Field Capacity	Full Saturation
q_{coarse} (W/m)	18.41	64	90.64
q_{fine} (W/m)	12.26	33.70	52.61
RPD between coarse and fine textures (%)	40.10	62.03	53.10

The effect of moisture content is discussed next. The numerical temperature distributions regarding dry, FC, and FS moisture contents of Ottawa sand and Richmond Hill clay-loam are presented in Figures 7.5 (a,b,c) and 7.6 (a,b,c), respectively. The quantitative comparison regarding the variation in moisture content is based on the below defined RPD between the heat flows of interest and its respective dry soil condition:

$$RPD = \frac{q_{\theta_2} - q_{\theta_1}}{\left(\frac{q_{\theta_2} + q_{\theta_1}}{2} \right)} \cdot 100\% \quad (7.5)$$

where q_{θ_1} and q_{θ_2} are the heat flows through the below-grade wall and the floor (BM-MN), for a moisture content θ_2 relative to θ_1 . The results in Table 7.2 demonstrate that moisture content has a strong influence on the heat transfer. For instance, the relative percentage difference between the dry and full saturation conditions of Ottawa and Richmond Hill soils can be as high as about

132% and 124%, respectively. It is clear that moist soils can cause much greater heat loss from a basement than dry soils.

Table 7.2: RPD in heat flow regarding variation of moisture content of Ottawa sand and Richmond Hill clay-loam.

	$\theta_1=\text{Dry}$ $\theta_2=\text{FC}$	$\theta_1=\text{Dry}$ $\theta_2=\text{FS}$	$\theta_1=\text{FC}$ $\theta_2=\text{FS}$
RPD between moisture contents of Ottawa sand (%)	110.64	132.47	34.45
RPD between moisture contents of Richmond Hill clay-loam (%)	93.30	124.40	43.82

Finally, the underground heat transfer is analyzed regarding the variation of thermal conductivity as a function of temperature. The problem is solved twice: first, on the basis of thermal conductivity being a function of temperature for the three moisture contents (Figures 7.5 (a,b,c) and 7.6 (a,b,c) for Ottawa and Richmond Hill soils, respectively), and then considering the thermal conductivity at a fixed temperature taken as an average of inside and outside temperatures, $T_{\text{ave}}=(T_{\text{inside}}+T_{\infty})/2$ for the three moisture contents (Figures 7.5 (d,e,f) and 7.6 (d,e,f) for Ottawa and Richmond Hill soils, respectively). As in the previous cases, the quantitative analysis regarding the temperature variation is based on the RPD as follows:

$$RPD = \frac{q_{\lambda=f(T,\theta)} - q_{\lambda=f(T_{\text{ave}},\theta)}}{\left(\frac{q_{\lambda=f(T,\theta)} + q_{\lambda=f(T_{\text{ave}},\theta)}}{2} \right)} \cdot 100\% \quad (7.6)$$

where $q_{\lambda=f(T,\theta)}$ and $q_{\lambda=f(T_{\text{ave}},\theta)}$ are the heat flows (per unit length in z direction) through the below-grade wall and floor regarding thermal conductivity as a function of temperature T for a moisture content θ , and of average temperature

T_{ave} for a moisture content θ , respectively. The results presented in Table 7.3 indicate that the assumption of thermal conductivity as a function of T_{ave} for a moisture content might lead to a significant error in heat transfer estimation (up to about 22% in the case of dry Richmond Hill clay-loam). But comparing with the effects due to soil texture and moisture content, the effect due to temperature is relatively insignificant.

Table 7.3: RPD between the heat flows regarding the thermal conductivity as a function of temperature and as a function of T_{ave} for three moisture contents ($T_{ave}=10^{\circ}\text{C}$).

Ottawa sand			
	Dry	FC	FS
$q_{\lambda=f(T,\theta)}$ (W/m)	18.41	64	90.64
$q_{\lambda=f(T_{ave},\theta)}$ (W/m)	16.19	60.25	77.57
RPD (%)	12.83	6.04	15.54
Richmond Hill clay-loam			
	Dry	FC	FS
$q_{\lambda=f(T,\theta)}$ (W/m)	12.26	33.7	52.61
$q_{\lambda=f(T_{ave},\theta)}$ (W/m)	15.28	36.27	46.39
RPD (%)	21.93	7.35	12.57

In conclusion, the numerical simulation showed that underground heat transfer is significantly influenced by soil thermal conductivity, which in turn depends primarily on texture, temperature, and moisture content. Over the ranges of parameters studied here, it appears that the moisture content has the most significant effect on underground heat transfer (up to 132% with respect to dry soil condition), followed by soil texture (up to 62% with respect to fine soil condition). Although the temperature has the least effect (up to 22% with respect to T_{ave} condition), it may become very significant if the temperature is high, say greater than 40°C , combined with moderately-to-highly moist soils ($\theta_{PWP} < \theta \leq \theta_{FS}$).

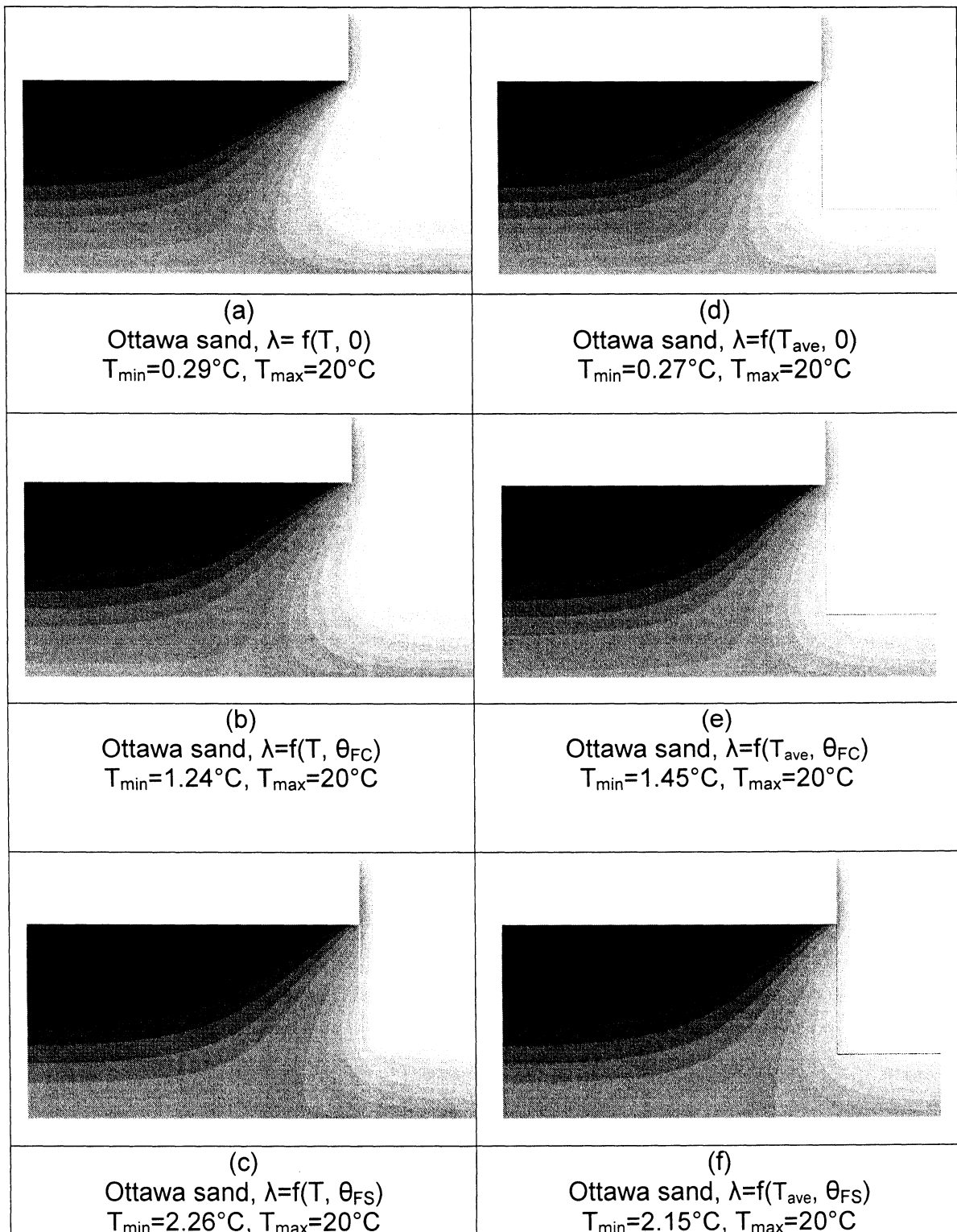


Figure 7.5: Temperature distributions for Ottawa sand at different moisture contents. For simulations (a), (b), (c) the thermal conductivity is set as a function of temperature for a moisture content ($\lambda = f(T, \theta)$), but in (d), (e), (f) as a function of T_{ave} for a moisture content ($\lambda = f(T_{\text{ave}}, \theta)$).

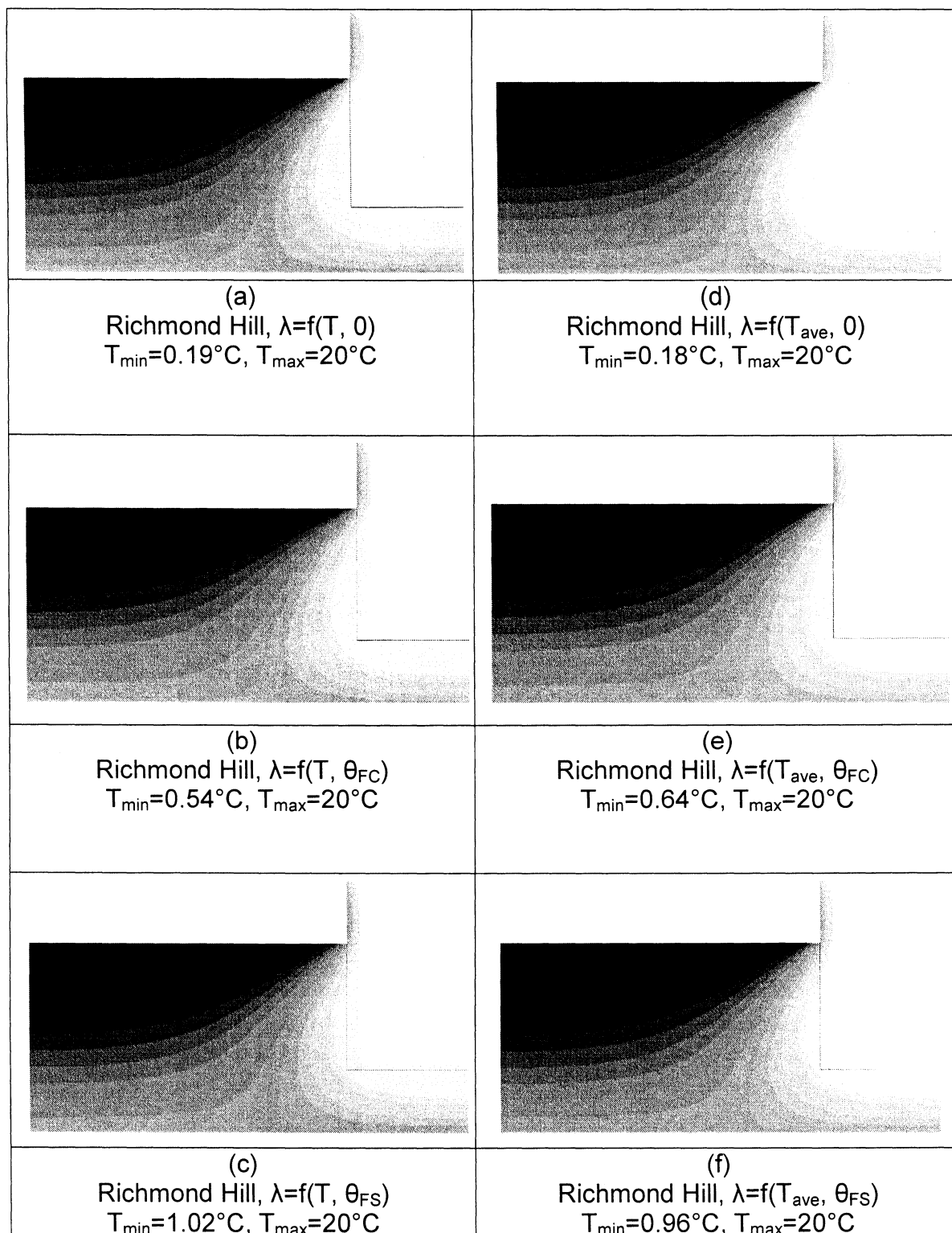


Figure 7.6: Temperature distributions for Richmond Hill clay-loam at different moisture contents. For simulations (a), (b), (c) the thermal conductivity is set as a function of temperature for a moisture content ($\lambda=f(T, \theta)$), but for (d), (e), (f) as a function of T_{ave} for a moisture content ($\lambda=f(T_{\text{ave}}, \theta)$).

CHAPTER

8

CONCLUSIONS AND RECOMMENDATIONS

8.1 Summary and Conclusions

This research was motivated by a need to obtain precise knowledge of soil thermal conductivity for a wide variety of engineering applications. Thus a study of the soil thermal conductivity was undertaken.

Firstly, the GHP apparatus and the data acquisition software have been modified, recalibrated and fine-tuned specifically for soil thermal conductivity measurements with the aid of a 2-D FEM numerical simulation of heat transfer within the apparatus including an experimental specimen for testing and validating the design modifications and experimental setup.

Secondly, a reliable and consistent sample preparation technique was developed for the cases of dry, barely-to-moderately moist and highly-to-fully saturated moist samples. The physical properties of soils were reported since without them the thermal data is meaningless.

Thirdly, two comprehensive sets of thermal conductivity for Ottawa sand (coarse soil) and Richmond Hill clay-loam (fine soil) were experimentally obtained using the guarded hot plate method, for temperature variation from 2 to

92°C and moisture content variation from complete dryness to full saturation with an overall measurement error associated with 95% confidence level of less than 3%, which, to the author's knowledge, is not yet available in the literature. After the completion of experiments the effects of temperature and water content on soil thermal conductivity were analyzed. The following is a summary of the findings:

- For both soils under investigation, the thermal conductivity varies in three stages with respect to increasing moisture content. At very low moisture contents up to the permanent wilting point, the thermal conductivity of soils increases slowly. As the moisture content further increases up to the field capacity, a rapid increase of the thermal conductivity can be observed. However when the field capacity is exceeded, the thermal conductivity either continues to increase with a lesser extent (for soil temperatures less than 72°C) or decreases gradually until full saturation (for soil temperatures greater than 72°C).
- Ottawa sand (coarse texture) has an average of 1.5 to 2.6 times higher thermal conductivities than Richmond Hill clay-loam (fine texture), corresponding from dry to fully saturated conditions, for all experimental temperatures.
- For low temperature range (2 ~ 30°C), the heat transfer is dominated by conduction through the moist soils with very limited extent due to vapour migration.

- However, vapour migration (i.e., mass transfer) plays a very critical role in heat transfer for high-temperature (greater than 40°C) and moderately-moist soils ($\theta_{PWP} < \theta \leq \theta_{FC}$), effecting a rapid increase in the thermal conductivity. In fact, for very high temperatures of 82 and 92°C, the peak thermal conductivity near the field capacity is even greater than the one at full saturation.

Fourthly, based on the gathered datasets, empirical correlations for soil thermal conductivity were developed as a function of moisture content for each experimental temperature and also as a function of both temperature and moisture content. The proposed correlations produced excellent fit to majority of the experimental data, and could be easily integrated into numerical analysis of underground heat transfer.

Fifthly, as an application example, one of the correlations was employed to evaluate soil thermal conductivity in a numerical study of underground heat loss from a basement. In particular, the study revealed that underground heat transfer is significantly influenced by soil thermal conductivity, which in turn depends primarily on texture, temperature, and moisture content. It was concluded that that the moisture content had the most significant effect on underground heat transfer (up to 132% difference with respect to dry soil condition), followed by soil texture (up to 62% difference with respect to fine soil condition). In the case considered, the temperature had the least effect (up to 22% difference with respect to constant thermal conductivity condition). However, it was suggested that its influence may become much more significant for high-

temperature applications beyond 40°C in a combination with moderately-to-highly moist soil conditions ($\theta_{PWP} < \theta \leq \theta_{FS}$).

8.2 Recommendations

One of the primary applications of the gathered datasets would be to aid the development of accurate analytical as well as empirical high-temperature models of soil thermal conductivity. Any existing models could be verified and possibly modified or recalibrated to improve their accuracy. An extension of this experimental study would be to measure the thermal conductivity of more soil types, namely, gravel, silt, clay and peat in unfrozen as well as frozen states, extending the minimum and maximum temperatures to around -20°C and 160°C, respectively (this may involve significant modification to the GHP apparatus and experimental container). The extended thermal conductivity datasets will allow precise verification and consequently improvement to any existing and future analytical and empirical models, and possibly lead to a universal methodology for evaluating soil thermal conductivity.

APPENDIX

A

**THERMAL CONDUCTIVITY OF EXPERIMENTAL SOILS WITH
TEMPERATURE AND VOLUMETRIC MOISTURE CONTENT**

Table A.1: Measured thermal conductivity (W/m·K) of Ottawa sand.

	VMC (m³/m³)	0	0.045	0.085	0.114	0.1352	0.1492	0.1631	0.183	0.27	0.333	0.366
T(°C)												
2		0.336	0.529	0.729	0.916	1.114	1.266	1.443	1.696	2.695	3.190	3.300
12		0.338	0.536	0.766	0.992	1.200	1.367	1.547	1.806	2.800	3.220	3.329
22		0.340	0.552	0.835	1.090	1.316	1.494	1.713	1.996	2.928	3.270	3.364
32		0.343	0.568	0.890	1.190	1.477	1.701	1.954	2.287	3.090	3.340	3.416
42		0.346	0.601	0.967	1.318	1.692	1.976	2.282	2.673	3.238	3.410	3.463
52		0.350	0.630	1.051	1.471	1.954	2.300	2.655	3.059	3.382	3.490	3.537
62		0.353	0.663	1.148	1.658	2.230	2.633	3.069	3.400	3.556	3.600	3.619
72		0.357	0.713	1.282	1.900	2.528	2.989	3.449	3.722	3.759	3.724	3.689
82		0.359	0.800	1.459	2.195	2.879	3.345	3.770	4.052	3.986	3.886	3.811
92		0.363	0.920	1.725	2.632	3.440	3.904	4.248	4.446	4.292	4.078	3.956

Table A.2: Measured thermal conductivity (W/m·K) of Richmond Hill clay-loam.

	VMC (m³/m³)	0	0.069	0.138	0.1706	0.2032	0.232	0.2684	0.302	0.3691	0.436	0.5035	0.571
T(°C)													
2		0.221	0.240	0.285	0.349	0.435	0.503	0.620	0.737	0.816	0.998	1.126	1.301
12		0.223	0.246	0.305	0.376	0.466	0.545	0.665	0.778	0.857	1.031	1.150	1.318
22		0.225	0.253	0.328	0.410	0.511	0.594	0.720	0.835	0.914	1.080	1.186	1.332
32		0.227	0.260	0.351	0.447	0.560	0.650	0.786	0.906	0.985	1.124	1.220	1.357
42		0.229	0.268	0.376	0.492	0.624	0.726	0.880	0.997	1.071	1.180	1.278	1.388
52		0.232	0.278	0.404	0.545	0.703	0.827	0.992	1.120	1.180	1.263	1.334	1.426
62		0.234	0.289	0.433	0.598	0.793	0.955	1.139	1.271	1.327	1.368	1.402	1.447
72		0.237	0.300	0.463	0.665	0.902	1.105	1.280	1.451	1.485	1.496	1.492	1.489
82		0.239	0.312	0.511	0.744	1.034	1.263	1.447	1.658	1.650	1.624	1.594	1.546
92		0.242	0.325	0.568	0.844	1.223	1.459	1.622	1.861	1.827	1.774	1.712	1.613

REFERENCES

- [1] Campbell, G., Jungbauer (Jr.), J., Bidlake, W., and Hungerford, R., *Predicting the Effect of Temperature on Soil Thermal Conductivity*, Soil Science, Vol. 158, No.5, pg. 307 – 313, 1994.
- [2] Shiozawa, S., and Campbell, G., *Soil Thermal Conductivity*, Remote Sensing Review, Vol. 5, pg. 301 – 310, 1990.
- [3] Gori, F., Corasaniti, S., *Theoretical Predictions of the Soil Thermal Conductivity at Moderately High Temperature*, Journal of Heat Transfer, Vol. 124, pg. 1001 – 1008, 2002.
- [4] Pourhashemi, A., Oliver, O., Hao, J., Ramesh, D., and Chawla, C., *An Experimental and Theoretical Study of the Nonlinear Heat Conduction in Dry Porous Media*, Int. Journal of Energy Research, Vol. 23, pg. 389-401, 1999.
- [5] Cote, J., Konrad, J., *A generalized thermal conductivity model for Soils and Construction Materials*, Canadian Geotech. Journal, Vol. 42, pg. 443-458, 2005.
- [6] Balland, V., Arp, P., *Modeling Soil Thermal Conductivities over a Wide Range of Conditions*, Journal of Environmental Engineering Science, Vol. 4, pg. 549-558, 2005.
- [7] Hiraiwa, Y., Kasubuschi, T., *Temperature dependence of thermal conductivity of soils over a wide range of temperature (5 – 75 °C)*, European Journal of Soil Science, Vol. 51, pg. 211-218, 2000.
- [8] Sorour, M., Mahmoud, R., *Thermal Conductivity and Diffusivity of Soil*, Int. Comm. Of Heat and Mass Transfer, Vol. 17, pg. 189-199, 1990.
- [9] Nusier, O., and Abu-Hamdeh, N., *Laboratory Technique to Evaluate Thermal Conductivity for some Soils*, Heat and Mass Transfer, Vol. 39, pg. 119 – 123, 2003.
- [10] Salmon, D., *Thermal Conductivity of Insulations using Guarded Hot Plates, Including Recent Developments and Sources of Reference Materials*, Measurement Science and Technology, Vol. 12, pg. R89 – R98, 2001.
- [11] Reid, D., *GHP Apparatus Design and Construction for Thermal Conductivity Measurements* MASC Thesis, Ryerson University, Toronto, Ontario, 2005.

- [12] Tarnawski, V. and Leong, W., *Thermal Conductivity of Soil at Very Low Moisture Content and Moderate Temperatures*, Transport in Porous Media, Vol. 41, pg. 137 –147, 2000.
- [13] Tarnawski, V., Gori, F., *Enhancement of the cubic cell soil thermal conductivity model*, Int. Journal of Energy Research, Vol. 26, pg. 143 – 157, 2002.
- [14] Abu-Hamdeh, N., *Measurement of the Thermal Conductivity of Sandy Loam and Clay Loam Soils using Single and Dual Probes*, Journal of Agricultural Engineering Res., Vol. 80 (2), pg. 209-216, 2001.
- [15] Naidu, A., Singh, D., *A generalized procedure for determining thermal resistivity of soils*, International Journal of Thermal Sciences, Vol. 43, pg. 43–51, 2004.
- [16] Sepaskhah, A., and Boersma, L., *Thermal Conductivity of Soils as a Function of Temperature and Water Content*, Soil Science Society, Vol. 43, pg. 439 – 444, 1979.
- [17] Campbell, S., Callissendor, C., Williams, H., *Probe for Measuring Soil Specific Heat Using a Heat Pulse Method*. Soil Science Society of America Journal, Vol. 55, pg. 291-293, 1991.
- [18] Black, W., Bush, R., and Martin Jr., M., *Soil Thermal Properties and Their Effect on Thermal Stability and the Rating of Underground Power Cable*, 7th IEEE/PES Transmission and Distribution Conference and Exposition, pg. 275 – 280, 1979.
- [19] Kasubuchi, T. Hiraiwa, Y., *Temperature Dependence of Thermal Conductivity of Soil*, Scientific Registration No. 435, 1997.
- [20] Hadas, A., *Problems Involved in Measuring the Soil Thermal Conductivity and Diffusivity in a Moist Soil*, Agricultural Meteorology, Vol. 13, pg. 105— 113, 1974.
- [21] Gangadhara Rao, B., Sing, D., *A Generalized Relationship to Estimate Thermal Resistivity of Soils*, Canadian Geotechnical Journal, Vol. 36, pg. 767-773, 1999.
- [22] Becker, B., Anil Misra, P., Fricke, B., *Development of Correlations for Soil Thermal Conductivity*, Int. Comm. of Heat and Mass Transfer, Vol. 19, pp. 59.68, 1992.
- [23] Kersten, S., *Thermal Properties of Soils*, Bulletin 28, Engineering Experiment Station, University of Minnesota, Minneapolis, 1949.

- [24] Gemant, A., *How to Compute Thermal Soil Conductivities*, Heating Piping and Air Conditioning, Vol. 24, No. 1, p. 122-123, 1952.
- [25] Johansen, O., *Thermal Conductivity of Soils*, Ph.D. thesis, Trondheim, Norway, (CRREL Draft Translation 637, 1977) ADA 044002, 1975.
- [26] De Vries, A., *The Thermal Conductivity of Soil*, Mededelingen van de Landbouwhogeschool te Wateninen, Vol. 52, No. 1, p. 1-73, translated by Building Research Station (Library Communication No. 759), England, 1952.
- [27] Van Rooyen, M., Winterkorn, H., *Structural and Textural Influences on Thermal Conductivity of Soils*, Highway Research Board Proceedings, Vol. 39, p. 576-621, 1957.
- [28] Farouki, T., *Thermal Properties of Soils*, Trans Tech Publications, 1986.
- [29] Salomone, L., William D., Kusuda, T., *Thermal Performance of Fine-Grained Soils*, Journal of Geotechnical Engineering, ASCE, Vol. 110, No. 3, pp. 359-374, 1984.
- [30] Salomone, L., William D., *Thermal Resistivity of Soils*, Journal of Geotechnical Engineering, ASCE, Vol. 110, No. 3, pp. 375-389, 1984.
- [31] Reid, D., Nikolaev, I., Leong W., Rosen, M., *Design and construction of a guarded hot plate apparatus for thermal conductivity measurements*, Proc. CANSOL, 2007.
- [32] Hollands K., "Direct measurement of gaseous natural convective heat fluxes," *Experimental Heat Transfer, Fluid Mechanics and Thermodynamics*, Shah et al. ed., Elsevier, New York, 160-168, 1988.
- [33] Moffat, J., *Describing the uncertainties in experimental results*, Experimental Heat Transfer Fluid Mechanics and Thermodynamics, Shah et al. ed., Elsevier, New York, pg. 3-17, 1988.
- [34] Klein, A., Beckman, A., Myers E., *FEHT Version 7.161*, F-Chart Software, 1996-2001.
- [35] Holton, R., Wirenga O., Nielsen, D., *A rapid technique for obtaining uniform water content distribution in unsaturated soil column*, Soil Science, Vol. 133, pg. 397-399, 1982.
- [36] Bligh P., Smith, C., *Apparent Thermal Conductivity Measurement of Soils in the Field and Laboratory - Using Thermal Conductivity Probe*, EEBS Report No. 25, US Department of Energy, Solar passive Division, 1983.

- [37] Dynatech Report, *The Apparent Thermal Conductivity and Thermal Resistance of Dry and Water Saturated Specimen of Ottawa Sand*. no. MIT-15a. Dynatech R/D Co.
- [38] Moench, F., Evans, D., *Thermal Conductivity and Diffusivity of a Soil Using a Cylindrical Heat Source*, Soil Science Society Journal, Vol. 34, pg. 377-381, 1969.
- [39] *Soil texture chart*, Soil Science Society of America, on web at <https://www.soils.org/>
- [40] Banin, A., and Amiel, A., *A correlation of the chemical physical properties of a group of natural soils of Israel*, *Geoderma*, Vol. 3, pp. 185–198, 1970.
- [41] Dahiya, I.S., Dahiya, D.J., Kuhad, M.S., and Karwasra, S.P.S., *Statistical Equations for Estimating Field Capacity, Wilting Point and Available Water Capacity of Soils from their Saturation Percentage*, *Journal of Agricultural Science*, Vol. 110, pp. 515-520, 1988.
- [42] Al Nakshabandi, G., Kohnke, H., *Thermal Conductivity and Diffusivity of Soils as Related to Moisture Tension and other Physical Properties*, *Agricultural Meteorology*, Vol. 2, pg. 271-279, 1965.
- [43] De Vries, A. *Some Remarks on Heat Transfer by Vapour Movement in Soils*, *Proceedings of the 4th International Congress of Soil Science*, Vol. 2, pp. 38-41, 1950.
- [44] STATISTICA version 7.0, StatSoft, Inc., 1984-2007.
- [45] Tarnavski, V.R., Leong, W. H., and Bristow, K. L., *Developing a Temperature-Dependent Kersten Function for a Soil Thermal Conductivity*, *International Journal of Energy research*, Vol. 24, pg. 1335-1350, 2000.

